A MICROFABRICATED RAPID DESALTING DEVICE FOR INTEGRATION WITH ELECTROSPRAYING TIP

A Thesis
Presented to
The Academic Faculty

By

Ivan Andres Tibavinsky

In Partial Fulfillment
of the Requirements for the Degree
Master of Science in the
School of Mechanical Engineering

Georgia Institute of Technology
August 2014

A MICROFABRICATED RAPID DESALTING DEVICE FOR INTEGRATION WITH ELECTROSPRAYING TIP

Approved by:

Dr. Andrei Fedorov, Advisor
School of Mechanical Engineering
Georgia Institute of Technology

Dr. Peter Kottke
School of Mechanical Engineering
Georgia Institute of Technology

Dr. Peter Hesketh
School of Mechanical Engineering
Georgia Institute of Technology

Date Approved: May 9, 2014

To my grandfather Hector Alejandro Bernal Soler

ACKNOWLEDGEMENTS

This work would not have been possible without the guidance and support from several people. I want to start by expressing my gratitude towards Dr. Andrei Fedorov. His advice, enthusiasm, and constant encouragement have been vital for my development as a researcher. I must also thank Dr. Peter Kottke, whose extensive knowledge and contributions were of immense importance to the development of this thesis.

Further, I am indebted to the staff at the Georgia Tech Institute for Electronics and Nanotechnology. In particular, Dr. Mikkel Thomas and Tran-Vinh Nguyen, who always went beyond expectations to provide help with sincere kindness when needed. Their assistance, patience, and friendship made the microfabrication of the presented device possible.

I also want to thank my lab mates, colleagues and fellow GT IEN cleanroom users for sharing knowledge through meaningful discussions and being a solid source of support and encouragement. They were very important to overcome difficult moments that inherently come while performing experimental research. I owe a great part of my learning experience to them.

Lastly and most importantly, I want to thank my parents, William Tibavinsky and Constanza Bernal. Without their sacrifices and efforts I would have never been able to attend a top caliber institution such as Georgia Tech.

TABLE OF CONTENTS

LIST OF TABLES

LIST OF FIGURES

ix

LIST OF SYMBOLS AND ABBREVIATIONS

MD	Microdialysis
ESI	Electrospray Ionization
MS	Mass Spectrometry
µTAS	Micro Total Analysis System
m/z	Mass-to-charge ratio
Cyt-C	Cytochrome C
DRIE	Deep Reactive Ion Etching
HPLC	High Performance Liquid Chromatography
SEC	Size Exclusion Chromatography
t	Sample residence time
V	Sample channel volume
Q_s	Sample volumetric flow rate
Δx	Control volume thickness
J''	Mass Flux
$C_{m,x}$	Concentration on left side of differential element
$C_{m,x+\Delta x}$	Concentration on right side of differential element
C_s	Sample fluid concentration
w	Sample channel width
t_m	Membrane thickness
$C_{m,b}$	Concentration at the membrane on buffer side
$C_{m,s}$	Concentration at the membrane at sample side

D_{eff}	Effective diffusion coefficient in membrane
h_s	Sample convective mass transfer coefficient
C_b	Buffer fluid concentration
h_b	Buffer convective mass transfer coefficient
R_s	Sample fluid mass transfer resistance
R_m	Membrane mass transfer resistance
R_b	Buffer mass transfer resistance
R_T	Total mass transfer resistance
v	Average sample fluid velocity
A_c	Sample channel cross sectional area
H	Sample channel height
Sh_s	Sherwood number in sample channel
Sh_b	Sherwood number in buffer channel
$D_{H,s}$	Hydraulic diameter of sample channel
$D_{H,b}$	Hydraulic diameter of buffer channel
D_i	Free diffusion coefficient of potassium chloride in water
ICP	Inductively Coupled Plasma
IPA	Isopropyl Alcohol
AMI	Acetone, Methanol, and Isopropyl alcohol rinse
SEM	Scanning Electron Microscope
AFM	Atomic Force Microscope
BOE	Buffered Oxide Etch
$\bar{h}_{s,x}$	Average mass transfer coefficient of sample channel over length

$\bar{h}_{b,x}$	Average mass transfer coefficient of buffer channel over length
P_s	Local pressure in sample channel
P_b	Pressure in buffer channel
κ	Permeability constant
A_m	Membrane area
ΔP	Difference between sample and buffer pressures
μ	Dynamic viscosity of water
DI	Deionized
$x_{fd,h}$	Hydrodynamic entrance length
$x_{fd,c}$	Concentration entrance length
Re	Reynolds number
D_h	Hydraulic diameter
Sc	Schmidt number
$\vec{U}$	Velocity vector
ρ	Density of water
C_∞	Free stream concentration

SUMMARY

Electrospray Ionization (ESI) is a technique that permits the soft ionization of large proteins and biomolecules without fragmenting them, which allows them to be characterized via Mass Spectrometry (MS). It has the potential of permitting the identification of transient intermediate products in biological processes in situ, which would provide great insight to researchers in the growing fields of proteomics and metabolomics. However, this application presents a technical challenge in that most relevant biochemistry occurs in aqueous solutions with high salt content, which makes successful identification of analytes by ESI-MS difficult.

This thesis presents the design, fabrication, and characterization of a microfabricated dialysis module that could alleviate this issue by desalting samples inline between sampling and electrospraying interfaces. Its small volume (~10 nL) minimizes sample transit time and, thus, optimizes ESI-MS analysis temporal resolution. A preliminary analytical model of dialysis elucidates the key performance parameters and sets the guidelines for consideration in its design. The device is then microfabricated in a cleanroom environment using techniques that have been well established by the microelectronics industry such as E-beam evaporation and Reactive Ion Etching. The system efficiency is demonstrated experimentally by assessing its salt removal effectiveness as a function of sample residence time. Mass spectrometry analyses of proteins in solutions with high salt content further corroborate its performance.

CHAPTER
1 INTRODUCTION

Great efforts in analytical chemistry have recently been dedicated to the miniaturization of procedures and techniques. The motivation for this endeavor has been, in part, the creation of compact integrated systems that perform several routine laboratory analyses using a single device. Microfabrication processes pioneered by the microelectronics industry are among the methods that have facilitated the development and even the batch fabrication of such systems, which are often called micro total analysis systems (µTAS) or lab-on-a-chip [1]. Beyond the convenience of parallelization of analyses and increased throughput, this technology has also made available the inherent improvements in many individual chemical processes that result when the dimensions of the device that performs them are minimized [2].

The aim of this project is to benefit from the increased speed of analysis that miniaturization offers to demonstrate the feasibility of fast biomolecule identification in biochemical liquid samples at ambient conditions. By Microdialysis (MD), the device developed separates salts from analytes in solution. Its small volume (~10 nL) permits minimization of fluid transit time.

The MD device is coupled to Electrospray Ionization (ESI), a technique that permits the ionization of a wide array of proteins and biomolecules and allows them to be identified via Mass Spectrometry (MS) [3]. This method is unique in that it allows the ionization of large molecules without fragmentation [4, 5] . ESI-MS has also demonstrated millisecond time resolved studies of solution-phase chemical reactions [6,

7]. However, commonly present salts that might render impossible mass analysis must be rapidly removed before electrospraying, which limits the ability to accomplish a similar task in *in situ* biological processes.

1.1 Electrospray Ionization Mass Spectrometry

ESI starts when an electric field is applied between a thin capillary, which contains a liquid sample that contains analytes of interest, and a counter electrode, as depicted in Figure 1.1. In the case of positive mode electrospray, the electric potential of the fluid in the capillary is positive with respect to the counter electrode. The strong electric field focused at the small tip of the thin capillary makes positive ions migrate towards the meniscus of the solution while negative ions migrate away from it [3]. The electrohydrodynamic forces that result from this process shape the surface of the solution into a Taylor cone. When the electric field becomes large enough, a jet of small positively charged droplets is emitted from the tip of the cone [5].The solvent in the droplets evaporates, which increases Coulombic repulsion between cations, and causes droplet fission. This fission and evaporation process is repeated in the smaller droplets until individual ions in the gas phase result from removal of electrons or adduct formations with protons and other cations.
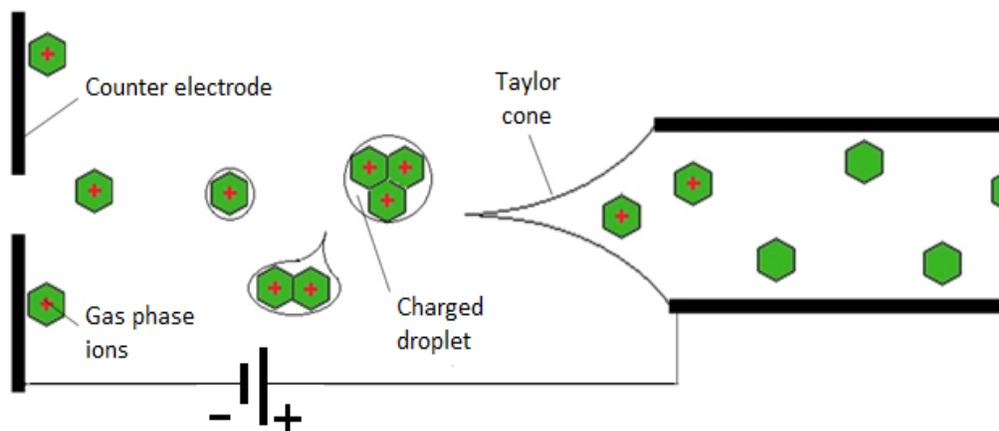
Figure 1.1 Electrospray Ionization process.

Once gas ions are obtained, a mass spectrometer analyzes their trajectory under a known applied electrical force, and by using Lorentz force law and Newton's second law of motion, their mass-to-charge ratios (m/z) are determined. The typical output of such a study is a mass spectrum, a plot of m/z values on the x-axis and their intensity on the y-axis. A relatively high intensity signals the presence of a molecule with the corresponding m/z value, but the exact magnitude depends on several characteristics of the electrospraying conditions and the particular analyte besides its concentration [5].

This method's convolution of ion charge and mass creates a need for charging to have a single dominant cause. The mass of a particular gas phase molecule uniquely determines its molecular formula if it is found with sufficient accuracy and precision, but in order to extract this information from mass spectrometry its charge must be found. Figure 1.2 shows the possible mass spectrum of a solution of glucose that was charged exclusively by protonotion. Its molecular weight is 180. The peaks at m/z = 181, 91, and 61 correspond to three possible analyte charge states caused by different adducts formed. Each peak has associated with it a group of peaks of smaller magnitude as shown by the

magnifications in Figure 1.3. These additional peaks correspond to less abundant isotopes, which explains their significantly lower intensity signal. Different isotopes in each group of peaks have atomic masses that differ by one atomic mass unit but have equal charge. As a result, the horizontal spacing between these peaks is inversely proportional to the charge of the molecule. For example, by enlarging the graph around $m/z = 91.0$, it becomes visible that the distance between the associated smaller peaks is 0.5, which corresponds to a charge state of 2.
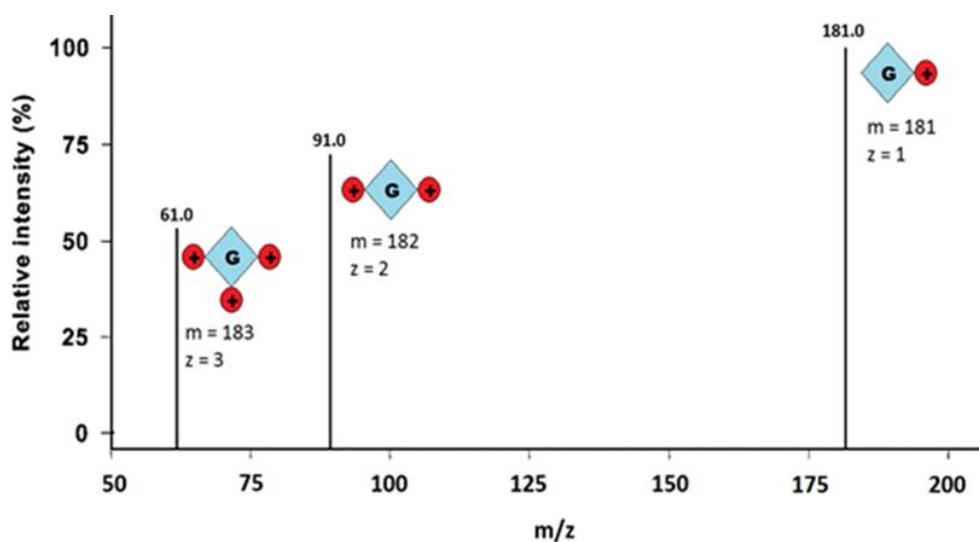
Figure 1.2 Representative ESI mass spectrum for glucose.
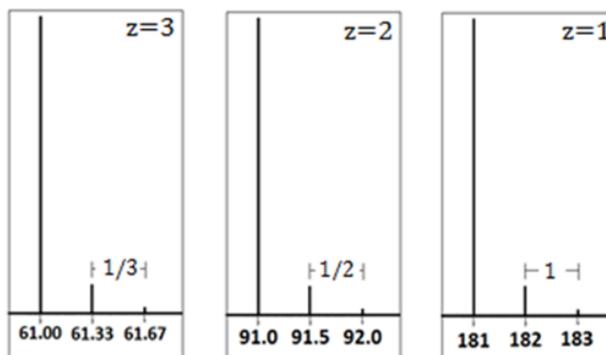
Figure 1.3 Magnification of the peaks in the representative glucose mass spectrum.

When salts such as sodium chloride or potassium chloride are also present, as often is the case in biological solutions, the cations that result from their dissolution also charge the analytes. Thus, analytes form a number of adducts in different combinations with other cations and not just protons, which significantly complicates the mass spectrum, and as a result, no clear relationship can be derived between the mass and the charge of a particle to identify it, as it is shown in Figure 1.4. This is the signal obtained from a solution of cytochrome complex (Cyt-C) without salt removal. As a comparison, Figure 1.5 depicts the ESI mass spectrum of the same sample of biological solution that underwent a desalination procedure that retained most analyte molecules.
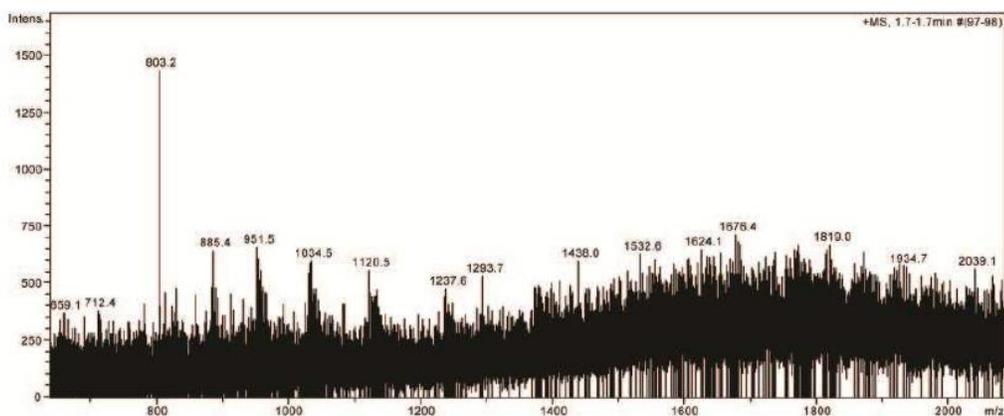
Figure 1.4 Mass spectrum of cytochrome c without salt removal [8].
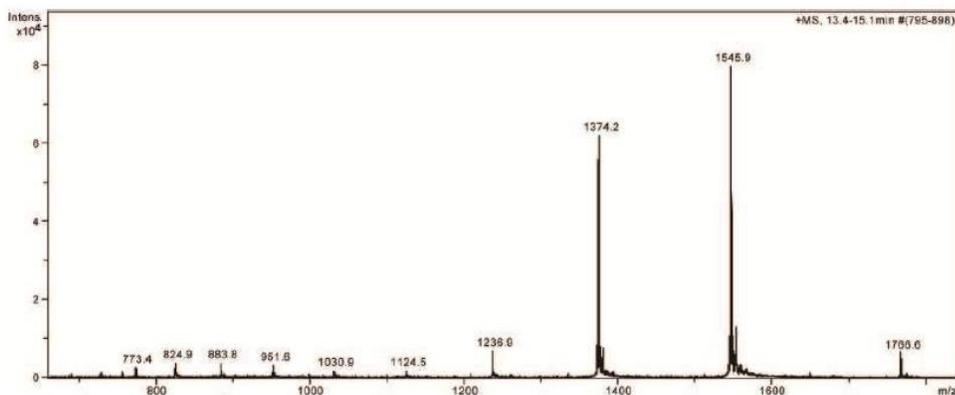
Figure 1.5 Mass spectrum of cytochrome c with salt removal by microdialysis [8].

The peaks that indicate the presence of an analyte of interest can only be discerned in this desalted sample. It is the ability to clearly identify a signal such as this one with transiently that motivates this work.

1.2 Current Methods

Numerous techniques to electrospray and desalt solutions exist, but few of them are adaptable to a system where these functions can be efficiently performed in-line in order to minimize the timescale at which molecules are transiently identified.

Electrospraying is usually obtained from pulled silica capillaries that are commercially available with internal diameters as small as 5 μm at the end [5]. These tips, however, are difficult to interface with separation devices. Some alternatives have been proposed using microfabrication techniques in an attempt to develop processes in which, both, electrospraying nozzle and sample preparing module can be produced monolithically. Besides making the connection between the electrospraying interface and other microfluidic components effortless, microfabrication also allows the production of electrospraying tips with smaller hydraulic diameters, which enables the electrospray process to occur at lower applied voltages [9]. Schultz et al., for instance, fabricated nozzles out of plane of a silicon substrate using deep reactive ion etching (DRIE), which resulted in tips that had a total volume of less than 25 pL [10]. Silicon substrate nozzles have also been made by etching small channels in a wafer, oxidizing it, and bonding it to another oxidized wafer. After opening the inlet and outlet of the channels and etching the silicon around the outlet, free standing oxide nozzles of rectangular cross section resulted [11]. A simpler approach was used by Ramsey et al. in which a sample was

electrosprayed directly from the end of a planar channel of a glass device [12]. However, since liquids tend to spread around the edge of a device if the channel outlet does not protrude beyond it, it can be very difficult to obtain stable electrospray with this method. 2D nib-like structures were also demonstrated to function as electrospraying sources by Arscott et al. [13]. These emitters were made by patterning SU-8 photoresist on a sacrificial layer, which was subsequently etched. Their compatibility with fabrication processes of other microfluidic systems was also demonstrated by monolithically integrating them with a micro chromatographic module [14].

Some chromatographic techniques are, in fact, widely used to desalt samples in-line in ESI-MS. High Performance Liquid Chromatography (HPLC) is, perhaps, the most common of these methods [15, 16], but Size Exclusion Chromatography (SEC) has also been demonstrated [17, 18]. Other processes include reversed-phase solid- phase extraction [19] and cation exchange [20]. However, all these methods share an inherent disadvantage in that they require either flow through a solid phase, which induces mixing, or an analyte adsorption-desorption cycle. These requirements make these techniques incompatible for time resolved chemical analysis.

Microdialysis (MD), on the other hand, allows analytes to be transported from sampling area to electrospraying interface directly without obstructions, which minimizes mixing. MD occurs when the high salt content sample flows through a channel that is separated by a porous membrane from another conduit through which a buffer solution flows. Since salts have a greater diffusion coefficient than analytes than the relatively large bioanalytes of interest in typical ESI-MS, they migrate by diffusion more readily from the sample to the buffer fluid. MD devices for ESI-MS applications typically

7

consist of tubular cellulose membranes sheathed by Teflon tubes [21-25]. While the sample flows through the cellulose membrane, the buffer fluid flows through the annulus between the membrane and the sheathing tube. A solid insert can be introduced in the membrane to enhance mass transfer in the sample channel [26, 27]. Different configurations have also been used. Xu et al. [28] laser cut serpentine channels in two polycarbonate chips, and sandwiched a dialysis membrane in between. This design was later improved by flowing the sample through a second chamber that was separated from the buffer by a lower molecular cut-off membrane [29]. Besides validating an alternative geometrical arrangement, these experiments demonstrated miniaturization of this technique. MD has, thus, been shown to have a great potential for fast in-line removal of salts in ESI-MS.

Due to its demonstrated effectiveness, versatility, and compatibility with high temporal resolution chemical imaging, MD is the desalting method of choice in this work. This thesis presents the design, fabrication, and characterization of a microfabricated system that performs this function and can be interfaced with an electrospraying tip. The goal is to obtain a system that demonstrates a significantly better performance than reported in previous works, which permitted chemical imaging of biomolecules with a temporal resolution of 1 minute [27]. Chapter 2 describes an analytical model of MD and explains how it was used to guide the device design. Chapter 3, then, details the system microfabrication and packaging, and how some of the steps of the process were developed. The experimental characterization of the final product is described in Chapter 4. Here the procedures to test device performance are outlined along with a refined model to analyze the data. Finally, Chapter 5 reports the progress made

towards integrating the device with electrospraying tips and recommends steps to

accomplish this goal. Suggestions for further improving device performance, and

concluding remarks are also made.

CHAPTER 2

ANALYSIS OF MICRODIALYSIS AND DEVICE DESIGN

In order to enable continuous high temporal resolution chemical imaging of biological solutions by Electrospray Ionization Mass Spectrometry (ESI-MS), salts must be rapidly removed from the sample while it is in transit from sampling point to electrospraying tip. Microdialysis (MD) has been shown to be a suitable desalting method for this purpose [19-27].

The scale of the sample residence time in an MD module, t, is determined by

$$t = V/Q_s \tag{2.1}$$

where t is the transit time, V is the total sample conduit volume, and Q_s is the sample volumetric flow rate. Since the sample flow rate is fixed by electrospraying conditions at approximately 30 μL/hr [9, 27], the total internal volume of the sample channel needs to be minimized to reduce residence time. In order to better understand how dialysis effectiveness is influenced by this requirement, an analysis based on the governing physical principles of MD separation was performed. The results are used along with consideration of the capabilities and limitations of the available materials and fabrication techniques to determine the important parameters to guide the design process.

2.1 Analytical Model

Figure 2.1 shows a control volume of thickness Δx. It encloses a differential element of a liquid sample that contains salt. The sample flows at a volumetric flow rate, Q_s, in a rectangular channel delimited at the upper boundary by a porous membrane. On the other side of this membrane a buffer fluid with no salt content flows in parallel. No bulk flow across the membrane is considered. Both flows are assumed to be hydrodynamically fully developed, laminar and steady-state. Applying the mass conservation principle to this element, Equation (2.2) results.

$$Q_s C_{s,x} = J'' w \Delta x + Q_s C_{s,x+\Delta x} \tag{2.2}$$

where J'' is the mass flux across the membrane, and w is the width of the sample channel. The relationship between the concentrations on the right and on the left side of the element, $C_{s,x}$ and $C_{s,x+\Delta x}$ respectively, can be approximated by a first order Taylor series expansion.

$$C_{s,x+\Delta x} = Q_s C_{s,x} + \frac{dC_s}{dx} \Delta x \tag{2.3}$$

By substituting this result in Equation (2.2), taking the limit as $\Delta x \to 0$, and simplifying, the following expression is obtained, where w is the width of the sample channel.

$$\frac{dC_s}{dx} = -\frac{J'' w}{Q_s} \tag{2.4}$$
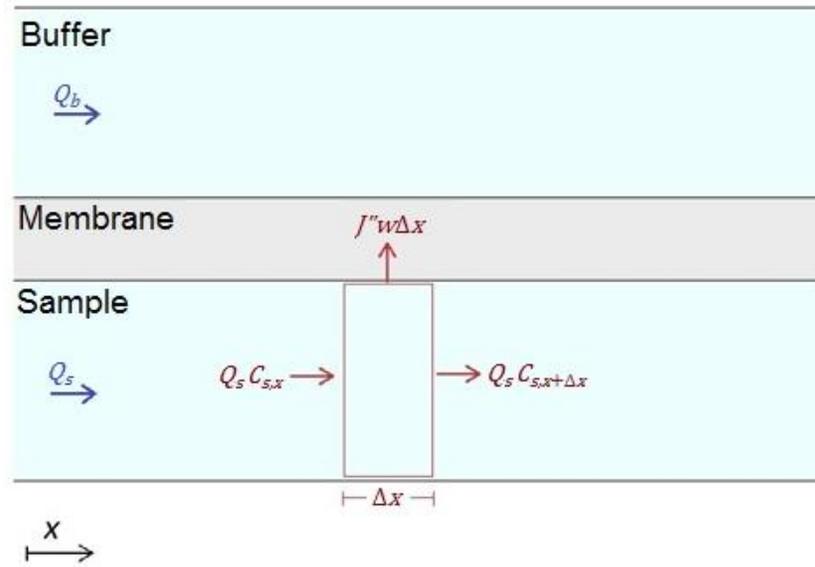
Figure 2.1 Differential element of sample flowing in microdialysis device.

Assuming no bulk flow across the membrane and diffusion only in the vertical direction, an expression for J'' can be obtained by using Fick's first law. At steady state the concentration profile in the membrane is linear:

$$J'' = -D_{\text{eff}}\frac{dC}{dy} = -D_{\text{eff}}\frac{C_{m,b} - C_{m,s}}{t_m} \qquad (2.5)$$

Here, t_m is the thickness of the membrane, and $C_{m,b}$ and $C_{m,s}$ are the local concentrations at the boundaries of the membrane at the buffer and sample sides, respectively. D_{eff} is the effective diffusion coefficient of the salts in the membrane.

Another expression for J'' can be obtained from convection mass transfer in the sample channel.

$$J'' = h_s(C_s - C_{m,s}) \qquad (2.6)$$

In this equation h_s is the local convective mass transfer coefficient in this channel, which under the assumptions of fully developed flow both hydrodynamically and in concentration, remains constant along the channel.

Assuming the buffer flow rate to be much greater than that of the sample, the average concentration of the salt in the buffer channel, C_b, can be assumed to be constant and negligibly small due to significant dilution. Taking this into account and applying convection mass transfer principles in the buffer channel, Equation (2.7) results.

$$J'' = h_b(C_{m,b} - C_b) = h_b C_{m,b} \tag{2.7}$$

where h_b is the local convective mass transfer coefficient in the buffer, which is also assumed to be constant.

From Equations (2.5) to (2.7) an electrical circuit analogy can be drawn, as shown in Figure 2.2. R_s, R_m, and R_b correspond to the mass transfer resistances in the sample channel, the membrane, and the buffer channel, respectively, and are defined in Equations (2.8) to (2.10).
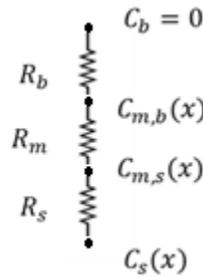
Figure 2.2 Electrical circuit analogy to mass transfer problem.

$$R_s = \frac{1}{h_s} \tag{2.8}$$

$$R_m = \frac{t_m}{D_{\text{eff}}} \tag{2.9}$$

$$R_b = \frac{1}{h_b} \tag{2.10}$$

The total resistance, R_T, is the sum of the three resistances mentioned above. From this knowledge, the local mass flux can be calculated as expressed by Equation (2.11), and by plugging this result into Equation (2.4) and integrating from the sample inlet to a position, x, in the sample channel, Equation (2.12) results.

$$J'' = \frac{C_s}{R_T} = \frac{C_s}{R_s + R_m + R_b} \tag{2.11}$$

$$C_s(x) = C_{s,i}\exp\left(\frac{-w}{Q_s(R_s + R_m + R_b)}x\right) \tag{2.12}$$

Here $C_{s,i}$ is the salt concentration in the sample fluid at the inlet of the channel.

The nature of the relationship between C_s and the time, t, that the sample spends in the device, permits a more direct evaluation of the performance of the system relative to the goal of this project. It can be obtained from Equation (2.12) using the following modification of Equation (2.1):

$$t = \frac{x}{v} = \frac{xA_c}{Q_s} = \frac{xwH}{Q_s} \tag{2.1}$$

Here v is the sample average velocity, A_c, is the cross sectional area of the channel, and H is its height. This results in Equation (2.13).

$$C_s(t) = C_{s,i} \exp\left(\frac{-t}{H(R_s + R_m + R_b)}\right) \tag{2.13}$$

2.2 Model-Based Device Design

A device design was determined from the information derived from the previous

analysis and assessment of the state of the art of fabrication methods and materials.

Equation (2.13) elucidates the parameters that are critical to device performance. The

total mass transfer resistance must be minimized along with the sample channel height, in

order to accelerate the decay of C_s with respect to t. This way, the residence time of the

sample is minimized while obtaining satisfactory desalting. Each of the individual

resistances was assessed to find an adequate compromise between fabrication feasibility

and device performance.

R_s and R_b are determined by the mass transfer coefficient in both channels, which

depends on the flow conditions and on the geometry of each of them. Since rectangular

ducts are most compatible with the planar nature of common microfabrication techniques,

only this geometry was analyzed. The Sherwood numbers in the sample and in the buffer

channels, Sh_s and Sh_b, determine the mass transfer coefficient in their respective

channels as follows:

$$h_s = \frac{Sh_s D_i}{D_{H,s}} \tag{2.14}$$

$$h_b = \frac{Sh_b D_i}{D_{H,b}} \tag{2.15}$$

where $D_{H,s}$ and $D_{H,b}$ are the hydraulic diameters of the sample and buffer channels

respectively, and D_i is the diffusion coefficient of the salts in the fluid. Under the

assumptions made in the analytical model, the Sherwood number in each of the channels

is constant throughout their entire length. In the sample channel, this constant

asymptotically approaches a maximum value as the aspect ratio, H/w, approaches 0

[30]. For this reason, the width of the channel was chosen to be significantly greater than

its height. However, by testing preliminary prototypes, it was found that when the

minimization of H/w, is exaggerated, attaining even flow across the width of the channel

becomes challenging and problematic bubbles that are difficult to remove form, as

depicted in Figure 2.3. A channel width of 100 μm was selected.
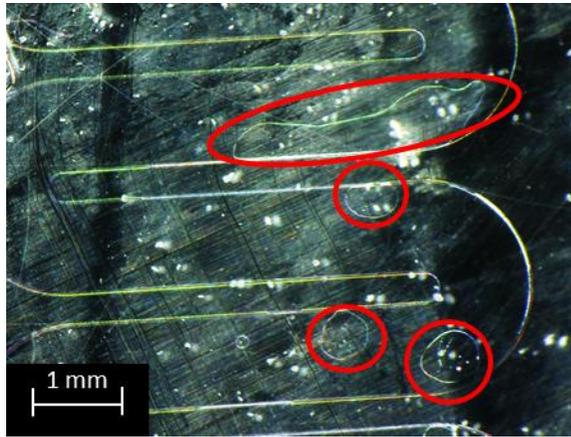
Figure 2.3 Bubble formations in sample channel.

In order to understand in detail how H affects device performance, all other

parameters were fixed at the values shown in **Error! Reference source not found.**, and

ffectiveness, as defined by Equation (2.16) was plotted as a function of residence time

using different values for channel height, as depicted in Figure 2.4. By comparing the

time it takes for 100% desalting to occur, the plot confirms the importance of minimizing

the channel height initially evident from Equation (2.13). This dimension was determined

to be 5 μm after an assessment of microfabrication methods revealed that this was close

to the limitations of practical techniques.

Table 2.1 Values used during parametric investigations.

Variable	Value
H	5 μm (when not varied)
$D_{H,b}$	100 μm (when not varied)
t_m	5 μm (when not varied)
w	100 μm
D_{eff}	5×10^{-10} m^2/s
$C_{s,i}$	300 mol/m^3

$$\% \text{ Effectiveness} = 100\% * \left(1 - \frac{C_s(t)}{C_{s,i}}\right) \tag{2.16}$$
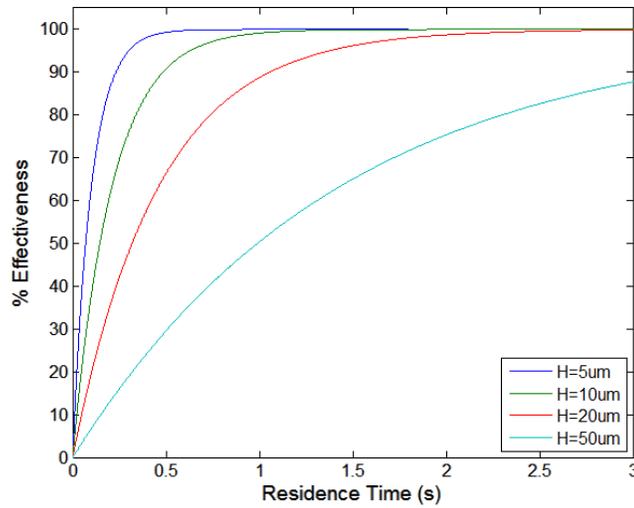
Figure 2.4 Device performance with different sample channel heights.

Having selected the values of H and w in this way, L was established to be close

to 16 mm after establishing the desired sample channel volume, V, in consideration that

this determines the sample residence time, as expressed in Equation (2.1). A previous

work that had similar objectives reported satisfactory desalting with a transit time of an

order of magnitude of 1 minute [27]. The aim of this project was, therefore, set to

improve this demonstrated capability, and completely remove salts an order of magnitude faster.

Even though minimization of the hydraulic diameter of both channels would be beneficial for device performance, as evidenced by Equations (2.14) and (2.15), in the interest of significantly simplifying the microfabrication process, the possibility of miniaturizing only the sample channel was studied. The consideration of this scenario is also justified by the fact that significantly higher flow rates would have to flow in the buffer channel to preserve a negligible salt concentration, which would cause a correspondingly greater pressure drop if the sizes of both channels were comparable. This pressure difference could potentially jeopardize the physical integrity of the system. With this motivation, the effect of the buffer channel hydraulic diameter on device performance was studied in the same way as the channel height with the same parameters outlined in Table 2.1. Figure 2.5 shows the results.
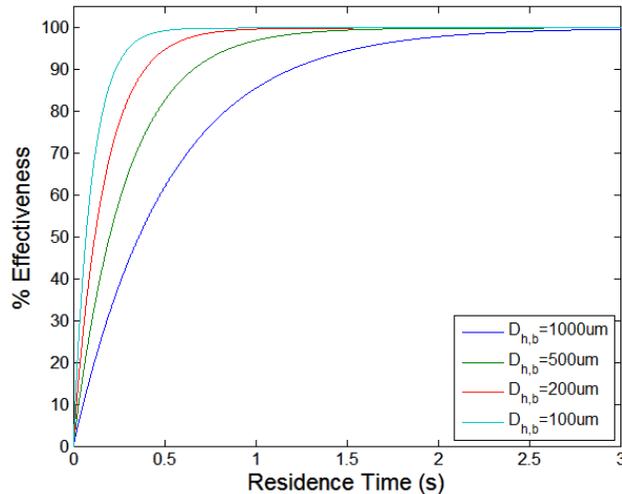
Figure 2.5 Device performance with different buffer channel hydraulic diameters.

Considering that the sample channel height was varied in the same proportions as the buffer channel hydraulic diameter, while all other parameters were equal, and comparing Figure 2.4 and Figure 2.5, it can be seen that the influence of $D_{H,b}$ on device performance is lower. For this reason, the dimensions of the buffer channel were mostly determined as was convenient to make microfabrication process and packaging possible.

Lastly, the role of the membrane thickness was investigated in a similar fashion also holding all other parameters equal at the values of Table 2.1. The results are depicted in Figure 2.6.
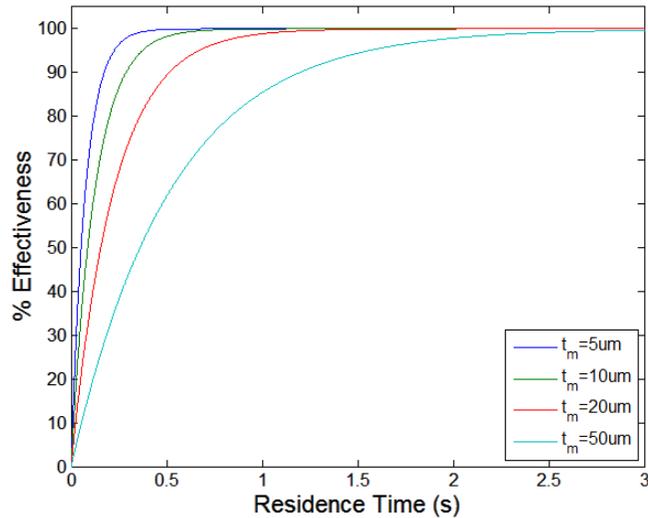
Figure 2.6 Device performance with different membrane thicknesses.

The magnitude of the influence of t_m on device performance is comparable to that of $D_{H,b}$, but minimizing this parameter has the additional advantage of facilitating a crucial step of the microfabrication process, as will be discussed in the next chapter. The only limit to the thinness of the membrane is related to its mechanical stability, which needs to be preserved through device fabrication, packaging, and testing. It was found with early device prototypes that the membrane is most likely to fail in this way during

experiments due to the differences in pressure drop between the sample and buffer channels.

The channel geometry can also be assessed in consideration of this regard. Serpentine channels, as used previously by other groups [28, 29], and shown in Figure 2.3 result in higher pressures at inlet of the sample channel, which requires a thicker membrane than if the channels were not curved. These considerations resulted in choosing the membrane to be close to 5 μm thick.

The discussed guidelines elucidate the fact that device performance is optimized, most importantly, by minimizing device dimensions. With this insight and consideration of the limitations of state of the art microfabrication techniques, the design parameters were established, as summarized in Table 2.1. The analytical model predicted the performance shown in Figure 2.7. Thus, it can be concluded that, in theory, close 100% salt removal is possible in less than 1 second.
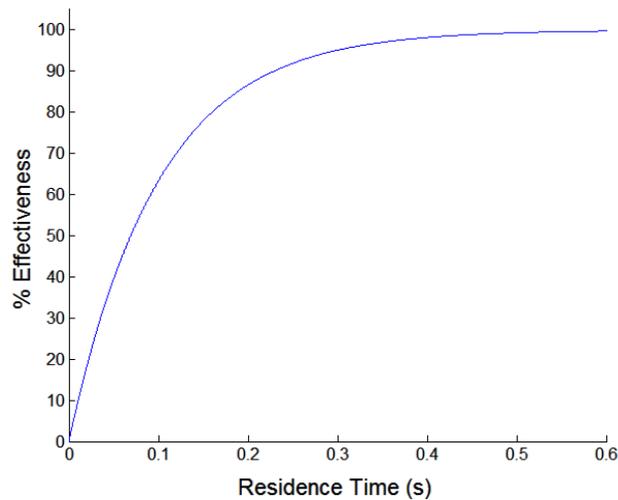
Figure 2.7 Expected device performance.

CHAPTER 3

DEVICE FABRICATION AND PACKAGING

With the guidelines set in Chapter 2, a microfabrication process flow for a microdialysis (MD) device was created. A procedure previously presented for a similar device [31] established the foundation, and the process was iteratively executed and modified to accommodate for the specific needs of the sample rapid desalting application until a final process flow and appropriate packaging were determined.

3.1 Device Description

The microfabricated device consists of a sample channel that has a rectangular cross section with a height of 6 µm and a width of 100 µm. A cross sectional view orthogonal to flow direction is depicted in Figure 3.1. The channel is defined on the lateral walls by SU-8 photoresist. A porous anodic alumina membrane that provides transport access to a buffer fluid outside of the channel constitutes the top wall. The bottom wall is a Pyrex substrate that allows visibility into the channel to monitor flow, and detect bubbles and possible contamination. High aspect ratio orifices in the silicon substrate provide an inlet and an outlet from the sample channel into fluidic interfaces.
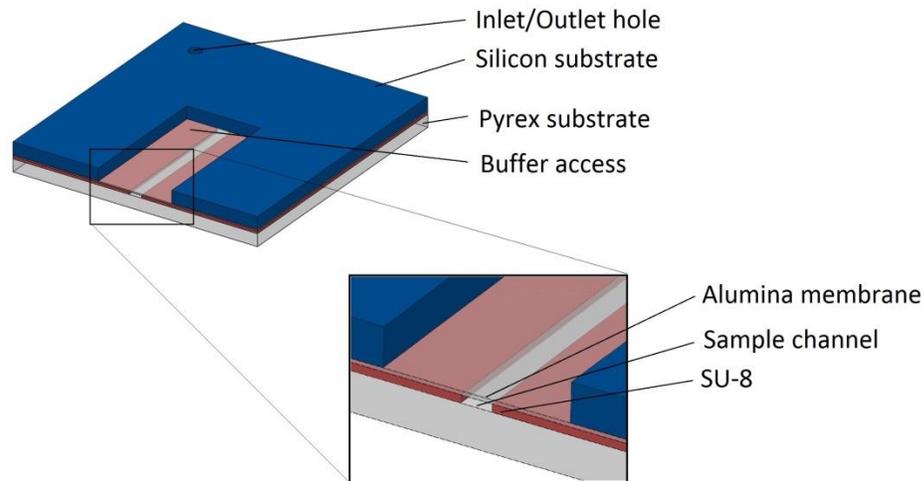
Figure 3.1 Cross sectional view of microdialysis device (not to scale).

3.2 Microfabrication of Microdialysis Module

Figure 3.2 illustrates the process flow of the microdialysis device fabrication. First, a double side polished 4 inch silicon wafer of (100) orientation was dipped in basic piranha at 120°C for 10 minutes (CMOS Cleaning Station), and subsequently spin dried with standard parameters (CMOS Spin Rinse Drier). Then, a 3 μm thick layer of oxide was thermally grown by wet oxidation at 1100°C for 18 hours (Tystar Poly Furnace) (Step 1). In order to define the inlet and outlet holes, which had a diameter of 60 μm, photolithography was then performed. Shipley's SPR 220 photoresist was spin-coated (250 rpm, 1000 rpm/s, 5s followed by 2000 rpm, 500 rpm/s,40 s) (BLE Spinner), and the wafer was baked at 110°C for 3 minutes. Then, the substrate was exposed to 500 mJ/cm^2 of 405 nm UV radiation (TSA Mask Aligner), and subsequently developed for 4 minutes in MF-319. After rinsing with deionized (DI) water, the photoresist within 5 mm from the edge of the wafer was removed with a swab dipped in acetone so that the substrate would

not stick to the clamp of the Plasma-Therm ICP. Then, the wafer was hard baked at 100°C for 15 minutes. This resulted in a 9 μm thick layer of photoresist.

1. Wafer wet oxidation
2. Inlet/outlet hole patterning in oxide layer
3. Ti/Al metallization
4. Al anodization

5. SU-8 application and patterning
6. Inlet/outlet hole etch

7. Bonding to pyrex wafer
8. Patterning of visible features
9. Buffer channel access patterning in oxide layer

10. Buffer channel access etch
11. Oxide and Ti etch
12. Pore opening

Silicon
Oxide
Aluminum
Alumina
SU-8
Pyrex

Figure 3.2 Microdialysis device fabrication process flow.

The pattern in the resist was then transferred onto the oxide layer by Inductively Coupled Plasma (ICP) etch with the parameters outlined on Table 3.1 (Plamsa-Therm ICP), and the photoresist was then stripped by rinsing it with acetone, methanol, and isopropyl alcohol (IPA) in that order. Rinsing with these solvents is also known as AMI (Step 2).

Table 3.1 Silicon oxide dry etch parameters.

| Pressure	5 mtorr
Ar flow rate	5 sccm
C_4F_8 flow rate	15 sccm
CO_2 flow rate	28 sccm
ICP power	800 W
Chuck power	40 W
Time	35 min

Following the inlet and outlet hole patterning on the oxide layer, the wafer was cleaned in 3:1 acid piranha for 15 minutes with no additional heat to the one produced by the exothermic reaction of the mixture. Then, a metallization of a titanium adhesion layer followed by an aluminum layer was performed by e-beam evaporation (CHA E-beam).

As discussed in Chapter 2, differences in pressure on either side of the alumina membrane during experimental testing of the MD device require the membrane to be several microns thick in order to maintain mechanical stability. Since typical microfabrication metallization techniques result in maximum thicknesses of hundreds of nanometers, the setup in the chamber of a CHA E-beam evaporation system was modified as shown in Figure 3.3. Four clamps were attached to the standard holder and a custom holder was attached to them with chains. As Figure 3.4 illustrates, up to four 100 mm silicon wafers could be attached to the custom holder with kapton tape. A 50 mm hole in the middle allowed material to be deposited on the crystal sensor of the tool, which was necessary to monitor and control metallization conditions during the process. In this manner, the substrates were suspended 30 cm away the source, which resulted in a deposition rate close to twice as high than if the standard holder had been used. As a

result, the metal layers deposited were significantly thicker than measured by the sensor of the tool, but the thickness uniformity across the wafer was significantly affected. The actual total thickness of both layers decreased along the diameter of the wafer from 7.2 μm at the flat to 4.4 μm at the opposite side. The final thickness and deposition rate of the titanium layer as measured by the sensor were 25 nm, and 1 Å/s respectively, and those of the aluminum layer were 2.5 μm, and 5 Å/s also as measured by the sensor (Step 3).
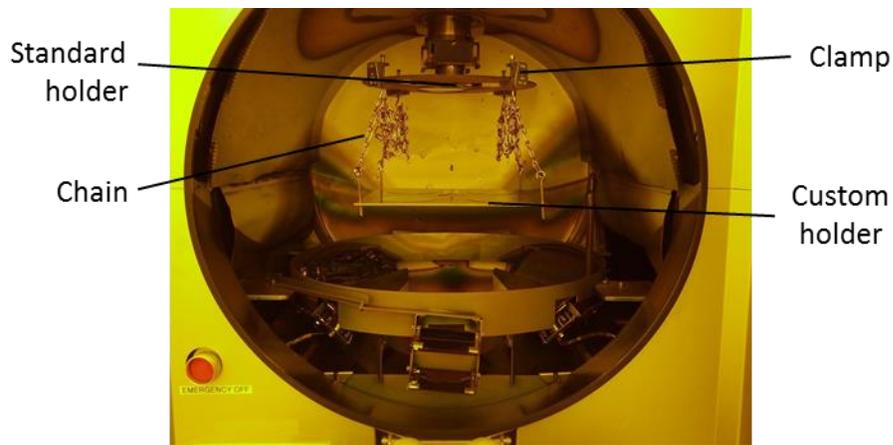
Figure 3.3 E-beam evaporation chamber during deposition of alumina precursor material.
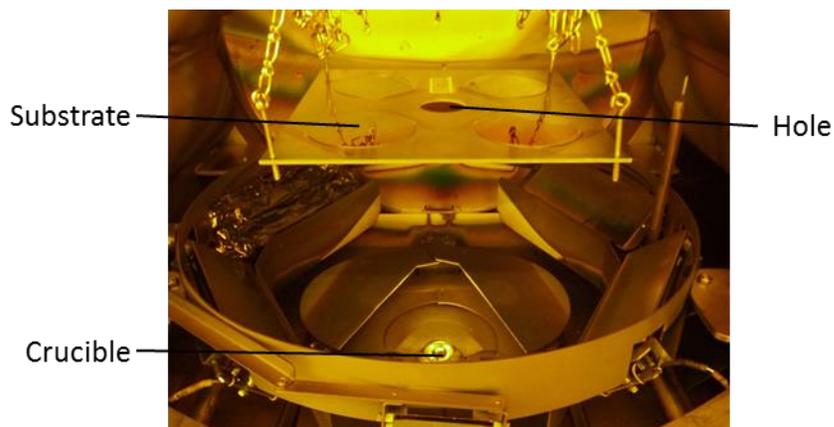
Figure 3.4 Custom substrate holder during deposition of alumina precursor material.

In order to fabricate the porous membranes, the aluminum was then anodized for 30 minutes in 2 L of 0.3 M oxalic acid at 0°C in a jacketed beaker that had a solution of ethylene glycol maintained at temperature by a recirculating chiller. A potential of 40 V with respect to a graphite rod about 30 cm in length and 3 mm in diameter was applied. The thin layer of alumina created during this step was then stripped by dipping the wafers in 1.5% chromic acid and 5% phosphoric acid at 65°C in order to expose the organized preferred nucleation points for the next anodization, which was performed with the same parameters as the first one for 6 hours to ensure complete anodization of the aluminum (Step 4). This process results in a structured material that consists of parallel cylindrical pores of length equal to the thickness of the alumina. A Scanning Electron Microscope (SEM) micrograph and a tapping mode atomic force microscope (AFM) scan of the surface are shown in Figure 3.5. The pores are approximately 50 nm in diameter. The porosity was determined using the manipulated micrograph in Figure 3.6. By calculating the ratio of black pixels to white pixels in the image, the proportion of pores-to-inactive area can be calculated. Since the pores are known to be parallel, the volume proportion was assumed to be equal. In this manner, it was determined that the pores comprise close to 25% of the membrane total volume.
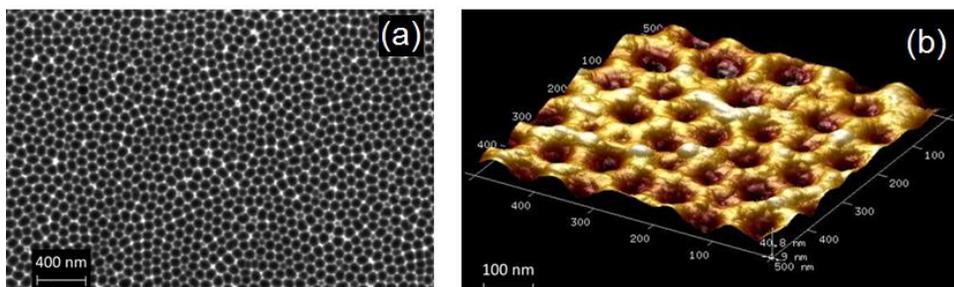
Figure 3.5 (a) SEM micrograph and (b) AFM tapping mode scan of alumina membrane.
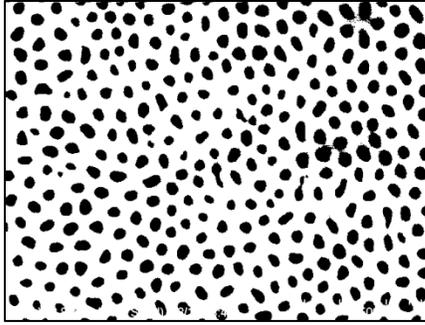
Figure 3.6 Manipulated alumina membrane micrograph used for porosity determination.

Following the creation of the alumina membrane, the wafer was squirted for at least five seconds with each of the AMI solvents. Then, a 6.5 μm layer of SU-8 3005 was spin-coated (250 rpm, 1000 rpm/s, 5s followed by 2000 rpm, 500 rpm/s,40 s) (BLE Spinner) on to the porous alumina side of the wafer, and subsequently, the substrate was baked at 95°C for 2 minutes and 30 seconds. Channels were patterned with backside alignment to pair up the ends of the channels to their inlets and outlets. The substrate was exposed to 225 mJ/cm^2 of 365 nm UV light (EVG Mask Aligner) and post-exposure baked at 95°C for 2 minutes and 30 seconds once again. Then, the resist was developed in SU-8 developer for 2 minutes, and subsequently rinsed with IPA only (Step 5). After this step and until bonding to a Pyrex substrate was performed, the wafer was not rinsed with any fluids other than IPA and care was taken to not expose the substrate to white light by covering it with aluminum foil whenever transportation out of a yellow light area was required.

The area within 5 mm from the border of the wafer was then lightly covered with cool grease on the side that had patterned SU-8 using a swab. A carrier wafer, which had 1 μm layer of silicon oxide, was firmly pushed against the wafer on the same side. In this manner, the two substrates were attached to each other for ICP etch of silicon. The

carrier wafer and the cool grease also served to protect the SU-8 from white light. On the side of the processed wafer that was still accessible, the perimeter of the wafer was covered with kapton tape to protect the areas from which oxide was unwantedly removed due to the removal of photoresist on the edges before performing Step 2. Alignment marks were also protected in the same way. The inlet and outlet sample channel holes were subsequently etched with 800 cycles of a Bosch process with the parameters outlined in Table 3.2 (STS ICP). After ensuring complete etch of the silicon by observing light through the holes, the tape on the borders and on the alignment marks was removed.

In order to remove the remaining membranes of oxide, titanium, and alumina at the bottom of the inlet and outlet holes, droplets of a 1 M solution of sodium hydroxide were carefully placed on the alumina side of the holes by pressing with a swab dipped in the solution to ensure that the fluid would make contact with the alumina. After 5 minutes, the droplets were carefully removed with a fresh swab, and then, the wafer was sonicated in an IPA bath for 10 minutes (Step 6). Complete opening of the holes was ensured by softly pushing the wafer against a hard surface coated with IPA. As expected, IPA visibly flowed through the holes.

Following the inlet/outlet hole opening, the substrate was bonded to a Pyrex wafer applying a pressure of 10 bar at a temperature of 130°C for 30 minutes (Step 7) (Obducat Nanoimprinter).

Table 3.2 Silicon etch parameters.

	Passivation	Etch
SF_6 flow rate	0	130 sccm
C_4F_8 flow rate	85 sccm	0
Coil Power	800 W	800 W
Platen Power	0 W	10 W
Pressure	0.1 mTorr	0.1 mTorr
Time	9 s	11 s

Visible features such as dicing lines were necessary in order to handle the devices and align them in the package when finished. These were made by patterning SPR 220 with the previous parameters on the side of the bonded substrate that had the inlet and outlet sample holes. Then, a layer of 25 nm of titanium followed by a 100 nm layer of aluminum was deposited by e-beam (CHA E-beam) on the patterned photoresist at the standard distance from the source, and then lift off was performed (Step 8).

Following the patterning of visible features, once again, SPR 220 was applied and patterned with the previous recipe on the side of the substrate that had the sample holes. This time, in addition to removing the photoresist close to the border of the wafer, care was taken to remove glue left over from the kapton tape applied before Step 6 in order to avoid the sample sticking to the Plasma-Therm ICP. Buffer access to the membranes was patterned on the oxide with the ICP etch described in Table 3.1(Step 9) (Plasma-Therm ICP). Leaving the photoresist that served as a mask to pattern the silicon oxide on the wafer, silicon was etched with 600 cycles of the ICP etch outlined in Table 3.2. (Step

10)(STS ICP). Since the photoresist was the mask for the etching of these bigger features, it was not necessary to cover the borders with kapton tape once again.

In order to remove the oxide and the titanium on the resulting alumina membranes, the photoresist on the borders of the wafer was removed, as before, and ICP etch was once again used with the parameters in Table 3.1 (Step 11) (Plasma-Therm ICP). Finally, the pores in the membranes were opened on the backside by dipping the wafer in 5% phosphoric acid at room temperature for 45 minutes (Step 12).

The application of photoresist after access to the channels had been open made channel clogging a common occurrence. Figure 3.7 shows the sample channel of a device in which this situation arose. The fabrication process, thus, usually ends by soaking the devices in acetone for as long as it is necessary for the channel to open, which can take between half an hour and 2 days.
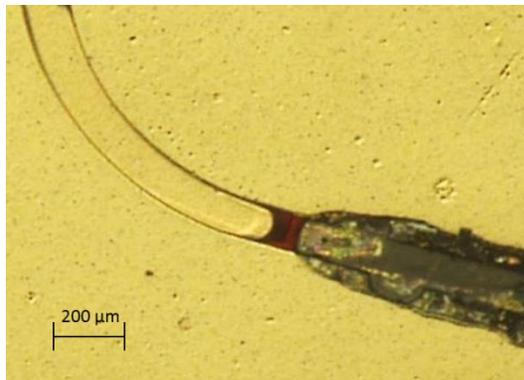
Figure 3.7 SPR 220 Photoresist clog in sample channel.

3.3 Determination of Process Procedures and Parameters

The process flow presented in Section 3.2 was the product of lessons learnt from a number of process executions. While success did not result from most of these, they did

serve to determine the adequate techniques and parameters that eventually led to the attainment of working devices.

3.3.1 Inlet/Outlet Hole Etch Mask and Etch Parameters

For instance, the inlet/outlet sample channel holes etch (Step 6) was first attempted using an SPR220 photoresist mask, as opposed to the silicon dioxide implemented in the final process. Despite the high selectivity between positive photoresist and silicon, a complete etch through the wafer was not accomplished before the photoresist mask was completely etched. This was due, perhaps, to redeposition of photoresist in the small features. Both, the etch standard recipe, described in Table 3.3, and the recipe in Table 3.2, were attempted using this photoresist mask, but results were unsatisfactory in both cases. However, the presence of photoresist was not a problem during access etch from the membrane to the buffer fluid (Step 10) due to the fact that the features etched during this step are significantly bigger.

Table 3.3 STS ICP standard recipe.

	Passivation	Etch
SF_6 flow rate	0 sccm	130 sccm
C_4F_8 flow rate	85 sccm	20 sccm
O_2	0 sccm	13 sccm
Coil Power	600 W	800 W
Platen Power	0 W	12 W
Pressure	10 mTorr	22 mTorr
Time	8 s	12 s

Even using a silicon dioxide mask, complete etch through the wafer was unsuccessful with the standard ICP etch recipe outlined in Table 3.3. Thus, of the

31

attempted combinations of mask and etch conditions, only a 3 µm thick silicon oxide and the parameters in Table 3.2, as described in Section 3.2, led to adequate results.

PECVD was also considered for production of the silicon dioxide layer during Step 1 of the process (Unaxis PECVD). Even though this method is significantly faster than wet oxidation, obtaining a uniform layer without pinholes was extremely challenging. The problem was exacerbated by contamination present in the chamber due improper cleaning. This issue caused through holes in unwanted locations of the wafer during inlet/outlet hole etch. Thermal oxidation reliably alleviated the problem and allowed the growth of an oxide layer on up to 25 wafers at the same time, which made the 18 hours (22 hours when taking into account ramping of the furnace) that the process requires a worthwhile time investment. Additionally, thermal oxidation grows a layer of oxide on the backside of the wafer as well, which is needed as an etch stop for both, Step 6 and 10 of the process.

3.3.2 Patterning of Silicon Dioxide

Alternatives for Step 2 of the process flow were also investigated. Silicon dioxide etch was attempted by RIE (Vision RIE and End-point RIE). Besides the etch rate being about 3 times lower (35 nm/min) than by ICP, the process had to be stopped and the chamber had to be cleaned three times before the process was completed, which created a time consuming inconvenience. For this reason, it was determined that an ICP system (Plasma-Therm ICP) would be better suited for the purpose of the MD device, despite the fact that satisfactory results were also obtained in this manner.

3.3.3 Creation of Porous Alumina Membrane

The successful creation of the porous alumina membrane was dependent on substrate cleaning prior to metallization, aluminum deposition, sample size, backside material removal, and pore opening.

During the first attempts of fabrication of porous alumina, no cleaning step was performed immediately before metallization. Later, when the aluminum was anodized, it appeared that the alumina or titanium layers delaminated from the substrate at several locations on the wafer. Cleaning in acid piranha prior to titanium and aluminum deposition solved the problem. As an alternative, a descum standard process (Vision RIE), outlined in Table 3.4, was also proved to yield satisfactory results.

Table 3.4 Vision RIE standard descum parameters.

Pressure	200 mTorr
Power	300 W
Temperature	25 ° C
O_2	50 sccm
Time	60 s

The distance of the substrate from the crucible during metallization was also found to have an impact in anodization results. Deposition of titanium and aluminum was, attempted at 20 cm, 30 cm, and 50 cm from the source. The thickness and deposition rate of the aluminum layer, as measured by the sensor of the tool, were 1 μm and 4 Å/s, respectively in every case. After anodizing the samples with the two step process described in the previous section, it was observed that organized pores did not form on the sample that was metallized at 20 cm from the source. This was due, perhaps, to differences in grain structure of the surface of the aluminum. In this manner, it was

33

determined that the optimal distance of the substrate from the source during this metallization step was 30 cm.

Initially, the anodization process was validated with the processing of small 1 mm × 2mm samples. When the process was first performed on a full 4-inch silicon wafer, it was found that results were unsatisfactory. This problem was attributed to localized temperature rises due to insufficient stirring of the electrolyte in proportion to the larger area of the substrate. For this reason, the 1-inch stir bar that had been previously used was replaced with one that had a length of 4 inches. Once this change was implemented, organized pores repeatably resulted once again.

During removal of silicon dioxide and titanium after the buffer access had been etched, more difficulties were encountered. A previous work [31] reported satisfactory removal of these two layers by exposure to Buffered Oxide Etch (BOE) without damage to the alumina membrane. However, when this procedure was emulated, it was found that the membrane was, in fact, significantly affected by this acid. For this reason, a dry etch was attempted. Since a C_4F_8 plasma etch had already been implemented with the parameters in Table 3.1, the same procedure was tested for the purpose of membrane backside material removal. Both layers were successfully removed in this manner without affecting the porous alumina membrane.

Finally, the adequate parameters for pore opening from the backside of the membrane had to be found. This procedure was first attempted using a 6% phosphoric acid solution at 65 º C. These specifications caused the membrane to rapidly dissolve entirely. A rinse of a 1M solution of sodium hydroxide was, therefore, attempted next, but this solution was found to affect the membrane even more rapidly than the previous

one. Success was finally attained by dipping the substrate in 6% phosphoric acid for 30 minutes at room temperature.

3.3.4 Bonding

Initially, bonding between the silicon and Pyrex substrates (Step 7) presented several difficulties, as well. During the first attempts, SU-8 was applied, soft baked, flood exposed , and hard baked on the Pyrex wafer with the same recipe used on the silicon wafer. This was done with the hope that an SU-8 – SU-8 interface would yield better results than an SU-8 – Pyrex interface. Using a Karl Suss SB6 Bonder system, combinations of temperatures between 130 º C and 250 º C, and pressures between 2 and 3 bar were applied for 2 hours on the wafers placed in contact at a surrounding ambient pressure of 1E-4 mbar. Easy visibility through the Pyrex wafer, allowed assessment of the results. It was determined that none of these attempts were successful. The Obducat Nanoimprinter was then used. The first attempt using this tool, was performed at 130 º C with an applied pressure of 10 bar (minimum applied pressure available on this system) for 30 minutes, as described in Section 3.2. These parameters yielded excellent results. No temperature ramping was necessary even though it is generally recommended for thermal cycling of SU-8. Later, it was observed that the same results were obtained when the Pyrex substrate did not have an applied layer of SU-8.

3.3.5 Step Execution Order

Despite having found parameters to each step of the microfabrication process that yielded satisfactory results, additional difficulties stemmed from performing them in inadequate order.

It was found, for example, that carrying out any processing steps between inlet/outlet hole opening (Step 6) and wafer bonding (Step 7) was challenging due to the fact that many of the processes occur with significantly different pressures on either side of the wafer. The through holes that allow flow into and out of the sample channel cause significant leaks. Even during a process as simple such as photoresist spin coating, it was found that the holes make it difficult to hold the wafer firmly to the chuck. This is due to the fact that the through holes make a vacuum seal impossible. Bonding to a Pyrex wafer satisfactorily covers these holes for the purpose of microfabrication processing.

It was also determined that avoiding any processing between aluminum anodization (Step 4) and application of SU-8 (Step 5) avoids contamination to the membrane. Although cleaning of the substrate in 3:1 acid piranha, as described in Section 3.2, was found to remove contaminants such as photoresist without, apparently, affecting the anodized alumina layer, successful devices did not result from substrates that required this procedure. The membrane might have been affected in ways that were not detectable by SEM or AFM.

By the same token, bonding should be performed as soon as possible after application and patterning of SU-8. Excessive evaporation of solvent or contamination on the surface of the photoresist may cause adhesion problems. However, a compromise had to be reached between this and the requirement to not apply photoresist after the inlet and outlet holes had been opened. For this reason, ICP silicon etch (Step 6) was executed after SU-8 patterning (Step 5) but before bonding (Step 7). Care was taken to perform these three steps within a period of 24 hours in order to attain acceptable results.

3.4 Packaging

A clear polycarbonate piece was machined to create a groove 0.5 mm in both depth and width in which a 1 mm thick silicone gasket of 30A hardness was inserted, as shown in Figure 3.8. The gasket was laser cut from a sheet of self-adhesive material using a Hermes LS500XL CO_2 Laser system in vector mode. Only one pass at 20% power and speed at 1200 DPI was necessary. The self-adhesive side was placed against the bottom of the polycarbonate groove. This gasket defined and sealed the outline of the buffer channel.

In order to make an adequate seal at the inlet and outlet of the sample channel, a recess 0.5 mm deep and 4 mm in diameter was machined on the polycarbonate. Then, a buna-n o-ring (1.1 mm ID, 3.6 mm OD) 1.27 mm wide was inserted in it. This piece was aligned on top of the microfabricated part, and tightly secured against another polycarbonate piece at the bottom with four hand-tight bolts and nuts. It was found that tightening with tools causes excessive pressure and generally breaks the microfabricated device. Figure 3.9 shows the assembly. Holes were drilled and tapped so that 1/4-28 thread fluidic connections to the sample and the buffer channels could be directly made on the polycarbonate using Idex Scientific nuts (P-202) and ferrules (P-200).
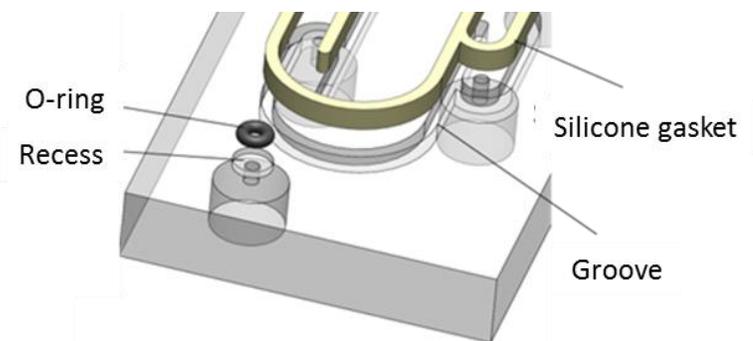

Figure 3.8 Machined part of polycarbonate package (not to scale).

37
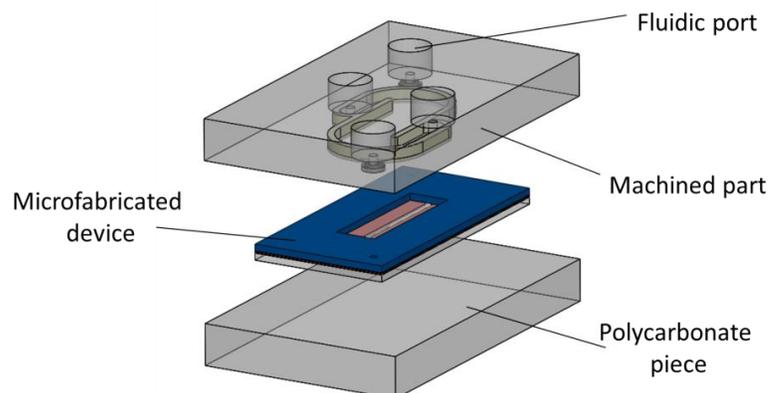
Figure 3.9 Package-device assembly (not to scale).

A different packaging approach was initially investigated in which commercial fluidic ports were glued onto a polycarbonate piece that had unthreaded holes. An MD device was sandwiched between this and another polycarbonate piece as in the final design. It was found, however, that the ports would inevitably detach from the polycarbonate piece after a few tests. The problem was solved by directly threading the fluidic junctions into the package.

An alternative for sealing sample channel fluidic connections and the buffer channel was attempted as well. A single planar gasket was sandwiched between the device and the polycarbonate piece to which the fluidic connections were made. This configuration was attempted with gaskets of hardnesses that ranged between 10A and 30A, and between 30 OO and 70 OO. Using some of these gaskets success was initially thought to have been obtained. However, after a few experimental runs, leaks rapidly developed that were very challenging to fix. Regardless of the material used, it was

difficult to obtain adequate sealing reliably in this configuration even when using self-adhesive gaskets.

Individual gaskets for buffer channel definition and sample channel access held in place by indentations in the polycarbonate alleviated the issue. However, it was important to ensure that the recesses in which the gasket and o-rings were inserted were thoroughly cleaned after machining. Occasionally, leaks were observed at the sample inlet between the polycarbonate and the MD device, but they were fixed by inserting the end of the plastic tubing in an o-ring, like the one previously described, after inserting the ferrule and before threading the connection into the polycarbonate. No leaks were observed thereafter.

CHAPTER 4

EXPERIMENTAL SYSTEM CHARACTERIZATION

The microdialysis (MD) device was designed optimizing key performance parameters and subsequently fabricated using state of the art techniques. The system was, thus, expected to remove salts effectively while requiring a low residence time. The device was tested with the procedures described in this chapter in order to characterize its performance. The experimental data obtained was found to be in disagreement with the model presented in Chapter 2, and therefore a more rigorous analytical prediction was developed to ensure that the physical principles that govern the system were understood. The MD device demonstrated removal of more than 95% of salts with a residence time of 1.2 seconds at flow rates close to those typically obtained during electrospray. Additionally, Electrospray Ionization Mass Spectrometry (ESI-MS) analyses confirm that the device facilitates the identification of proteins in solutions with high salt content, as was the goal of this project.

4.1 Microdialysis Experiments

The device was first tested by forcing a salt solution through the sample channel and deionized water through the buffer channel. The salt solution was collected at the sample outlet, and its concentration was measured. By assessing the change in salt concentration in the solution after treatment with the system, the effectiveness of the device was characterized.

4.1.1 Experimental Procedure

Figure 4.1 shows the schematic of the experimental setup used for the MD experiments.
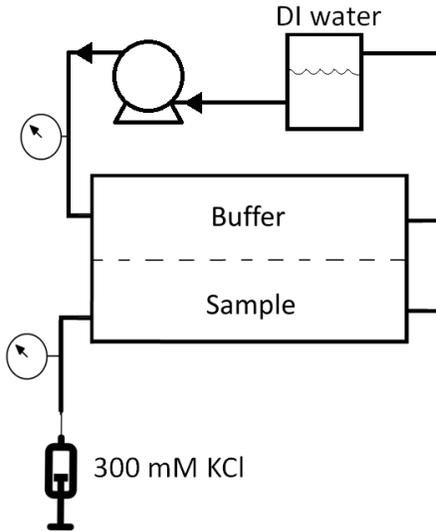

Figure 4.1 Microdialysis experimental setup schematic.

DI water from a large reservoir (~800 ml) was pumped through the buffer channel with a peristaltic pump (Watson-Marlow 205U) that was set to run at 50 rpm. Using a 0.025" bore tube (Watson-Marlow 982.0063.000) this rotational speed generated a flow rate of 50 ml/hr. The pressure in the line between the pump and the device was monitored with a microfluidic pressure transducer (LabSmith uPS0800-T116). In the sample channel, a 300 mM solution of KCl was introduced with a syringe pump (KD Scientific 100) at flow rates ranging from 30 to150 μl/hr. The pressure in the sample inlet line was also monitored with a similar device to that used in the buffer (LabSmith uPS0800-C360), and it was found to vary proportionally to the flow rate from 160 kPa at 30 μl/hr to 800 kPa at 150 μl/hr. The sample was collected at the outlet well, which was covered

during each experimental run to prevent the solvent in the sample from evaporating. Otherwise, the measured concentration would have been higher than it was right after exciting the device.

Initially, both channels were constantly observed to detect bubbles that would cause lower performance and non-repeatable data. Figure 4.2 depicts a microscope photograph that was taken while the sample channel was being monitored. However, it was consistently found that after the system had been running for a few minutes the bubbles that were initially present were carried away by the fluid, and that no new bubble formation occurred afterwards.

Figure 4.2 Bubble in sample channel.

4.1.2 Concentration Measurements

A common method to determine concentration of ionic substances in solution is by resistivity measurement. However, the small samples collected during experiments due to the low volumetric flow rates required excessive dilution in order to accommodate an average sized probe. For this reason, sample final concentration was measured using argentometric titrations.

This technique only measures the content of chloride in a sample, but the potassium ion was assumed to be present in the same amount. The Mohr method, the one used in this study, uses potassium chromate as the indicator and silver nitrate as the titrant. As shown in Figure 4.3, the procedure starts by adding a known volume of sample to be tested to the indicator solution, which is characterized by a bright yellow color. Small amounts of titrant at a known concentration are, then, slowly added to the solution. The silver nitrate preferentially reacts with the chloride ion forming a white precipitate. Once the free chloride ions are depleted due to this reaction, the titrant that is further added reacts with the potassium chromate forming a red solid. The appearance of the red color signals the endpoint of the titration, and since the volume and concentration of the titrant added are known, the concentration of the sample can be calculated.

$+ AgNO_3 \Rightarrow$ $+ AgNO_3 \Rightarrow$

K^+ Cl^-
K_2CrO_4 $Ag^+ + Cl^- \leftrightarrow AgCl(s)$ $2Ag^+ + CrO_4^{2-} \leftrightarrow Ag_2CrO_4(s)$
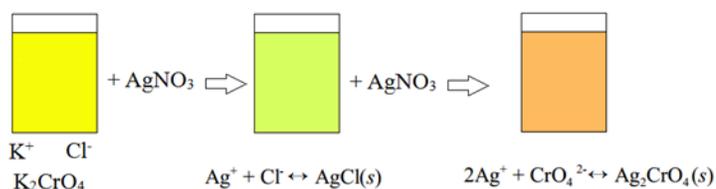
Figure 4.3 Argentometric titration procedure.

This method has a disadvantage in that it is very susceptible to human error. Since the endpoint of the titration is signaled by a subjective change of color of the solution, there is ample room for error. The problem was exacerbated by the fact that the volumes of the samples tested in this case were unusually small due to the small flow rates used in the experiments. However, a procedure was developed in which the relative presence of the species involved was optimized to make the change in color more easily distinguishable.

In order to test a sample treated with the MD device, first, 30 μl of dialyzed sample are added to a 2 ml cuvette in which 250 μl of a commercial solution of potassium chromate (Hach 1057-66) have been diluted in 500 μl of DI water. In parallel, 1 ml of 300 mM potassium chloride is added to a second cuvette in which the same mixture of indicator and water has been prepared. A small amount of titrant is added to this second cuvette to produce the turbid yellow color that characterizes the solution before the endpoint is reached. A digital titrator (Hach 1690001) is used to dispense small measured amounts of 0.025 N silver nitrate to the cuvette to which the sample to be measured was added, and the color of this solution is compared to that of the second cuvette at the same time. This comparison facilitates the determination of the endpoint of the titration.

The error of this method was statistically determined with a blind experiment. Six solutions of potassium chloride at different concentrations ranging from 20 to 250 mM were tested several times in such a way that the tester had no previous knowledge of the salt content of each sample. It was found that the relative error increases as the sample concentration increases. This is due to the fact that at higher salt content more of the white substance that results from the reaction of the titrant and the free chloride ions makes the solution more turbid, which makes identifying the endpoint more difficult.

4.1.3 Comparison of Results with Device Design Model

Using the method described above, the concentration of samples dialyzed at different flow rates was measured. The results obtained are shown in Figure 4.4. The y-axis corresponds to effectiveness as defined by Equation (2.16), and the x-axis

corresponds to the residence time of each of the samples, which is calculated from the flow rate and knowledge of the geometry of the device using Equation (2.1). The prediction by the preliminary model described in Chapter 2 is also shown for comparison.
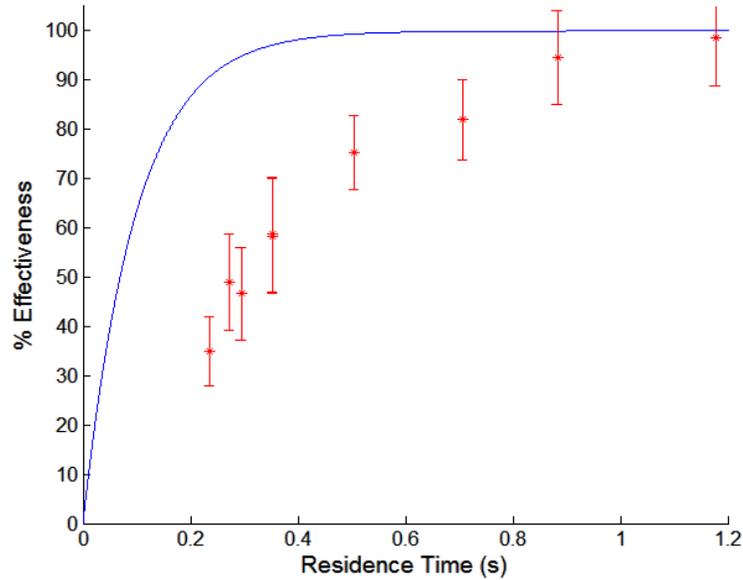

Figure 4.4 Comparison between dialysis experimental results and preliminary model.

The data demonstrates that salt removal is more effective with longer residence time, as expected, and it follows the same general trend as the model, which suggests that the analytical approach to understanding the device is appropriate. However, the analysis significantly over predicts performance.

Additionally, it was observed during experiments that the flow rate at the sample outlet was sometimes lower than at the inlet. This was most likely due to the large differences in pressure measured at the inlet of the two channels, which were as high as 800 kPa, and could have caused cross flow in the membrane. These observations led to a thorough revision of the assumptions made in Chapter 2 in order to ensure that the physical principles that govern the device were still understood.

4.2 Microdialysis Refined Model and Results

In the preliminary model it was assumed that cross flow across the membrane from one channel to another was negligible, but experimental observations suggested that it might have been substantial enough to affect results. For this reason, the permeability of the membrane was characterized experimentally, and a new analysis was performed.

Further scrutinizing initial assumptions, it was also realized that the uncommon geometry of the buffer channel in the device might cause a flow profile that is more difficult to characterize than initially thought. A computational model was, therefore, developed to predict the convective mass transfer coefficient in this fluid more accurately.

4.2.1 Membrane Hydraulic Resistance Measurement

The value of a membrane permeability constant, κ, as defined by Equation (4.1) was estimated with the setup represented by the schematic in Figure 4.5.

$$\kappa \equiv \frac{Q_{cross}}{A_m \Delta P} \tag{4.1}$$
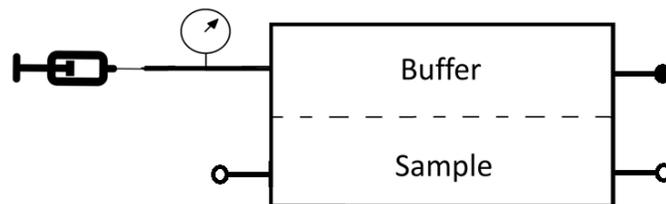
Figure 4.5 Experimental setup for membrane hydraulic resistance characterization.

In the above equation, Q_{cross} is the flow rate across the membrane caused by an uniform pressure difference between the two channels, ΔP, and A_m is the total membrane area.

The buffer chamber was filled and a constant pressure was applied to it to force flow into the sample channel. While cross flow is believed to occur mostly in the opposite direction during experiments, the hydraulic resistance was measured in this way because, once filled, the buffer can be more easily observed to detect bubbles that would give erroneous results, and if detected, they can be more easily removed.

A 1 ml syringe containing DI water was connected to the inlet of the buffer channel, and the outlet was closed. Both, the inlet and the outlet of the sample channel were left open, and the entire channel was assumed to remain at ambient pressure. The pressure in the line from the syringe to the buffer inlet, which was assumed to be the same as in the entire buffer chamber, was constantly monitored with a microfluidics pressure transducer (LabSmith uPS0800-T116) as a constant force was applied to the syringe. This line consisted of PEEK tubing, which has a low elastic yield.

Using Equation (4.1) , κ was calculated by taking Q_{cross} to be the change in volume observed in the syringe over the duration of the experiment, which was found to be 120 μL , divided by 10270 seconds, the time over which the force was applied. The membrane area, A_m was known to be 1.635E-6 m^2 from the device geometry. ΔP was 619 kPa, the average value of the constantly monitored pressure, which is plotted in Figure 4.6 as a function of time. This resulted in a κ value of 1.15E-11 m/s-Pa
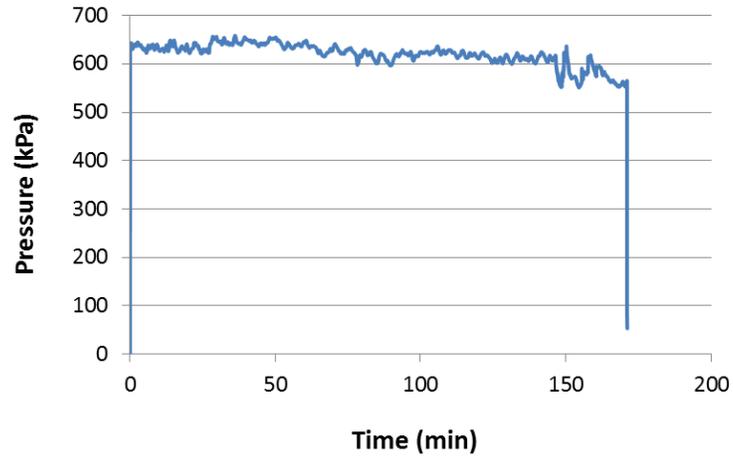
Figure 4.6 Measured pressure at buffer inlet as a function of time.

While some error might have resulted from the possible presence of undetected bubbles in the fluidic junctions and from a possible pressure gradient in the sample channel when filled, this method was still assumed to give a reasonable approximation of the membrane hydraulic resistance for the purposes of this work.

4.2.2 Refined Model

Having obtained insight on the magnitude of the cross flow of the device, a new model was derived. The analysis begins with the domain and the element depicted in Figure 2.1. Considering the change in concentration and also the change in flow rate between the left and the right sides of the element, the mass conservation equation becomes:

$$Q_s \frac{dC_s}{dx} + C_s \frac{dQ_s}{dx} = -J''w \qquad (4.2)$$

48

In order to find mass flux, J'', it was first found that advection in the membrane is not a significant component of mass transfer. A low Peclet number, Pe, as expressed in Equation (4.3), where D_i is the free diffusion coefficient of the species in solution, justified this assumption .

$$Pe = \frac{t_m v}{D_i} \tag{4.3}$$

The fluid velocity, v, was conservatively calculated from using the highest ΔP at the channel inlets observed during MD experiments (~800kPa) in Equation (4.1), as follows:

$$v = \frac{Q_{cross}}{A_m} = \kappa\, \Delta P \tag{4.1}$$

This resulted in a velocity of 9.2E-6 m/s, which gave a Peclet number of 0.023. This makes the assumption of negligible advection valid. This way, the expression becomes:

$$J'' = \frac{C_s}{\dfrac{1}{h_{s,x}} + \dfrac{t_m}{D_i} + \dfrac{1}{h_{b,x}}} \tag{4.4}$$

where $h_{s,x}$ and $h_{b,x}$ are the local convective mass transfer coefficients of the sample and buffer channels.

As expressed in Equation (4.5), the sample flow rate gradient along the channel is proportionally related to the difference between the local channel pressure, P_s, and the constant buffer channel pressure, P_b, by the permeability constant, κ, that was experimentally measured.

$$\frac{dQ_s}{dx} = -\kappa \, w (P_s - P_b) \tag{4.5}$$

Finally, the pressure gradient along the channel can be approximated by the equation for forced flow between parallel plates, where μ is the dynamic viscosity of the fluid [32]:

$$\frac{dP}{dx} = -\frac{12 \, \mu \, Q_s}{w \, H^3} \tag{4.6}$$

4.2.2 Determination of Convective Mass Transfer Coefficients

As part of the revisions to the assumptions originally made, the hydrodynamic and concentration flow profiles were evaluated considering the geometry of the device. The hydrodynamic an concentration entry lengths, $x_{fd,h}$ and $x_{fd,c}$ for the sample channel can be approximated with Equations (4.7) and (4.8), respectively [33].

$$x_{fd,h} \approx 0.05 \, Re_s * D_{H,s} \tag{4.7}$$

$$x_{fd,c} \approx 0.05 \, Re_s * D_{H,s} * Sc \tag{4.8}$$

Re_s is the Reynolds number of the flow, and Sc is the Schmidt number. Each of these have a value of 0.53, and 502 , respectively. This yields a hydrodynamic entry length of 0.95 μm and a concentration entry length of 0.5 mm. Both of these are small when compared to the channel length of 16.35 mm. This justifies the use of a constant convective mass transfer coefficient in this channel for the necessary calculations.

The buffer channel, on the other hand, required a more sophisticated method. Due to the uncommon geometry that resulted from the packaging of the device, as is shown in

Figure 4.7, a computational approach was necessary to calculate the mass transfer

coefficient. The fluid path is in the setup is shown with black arrows.
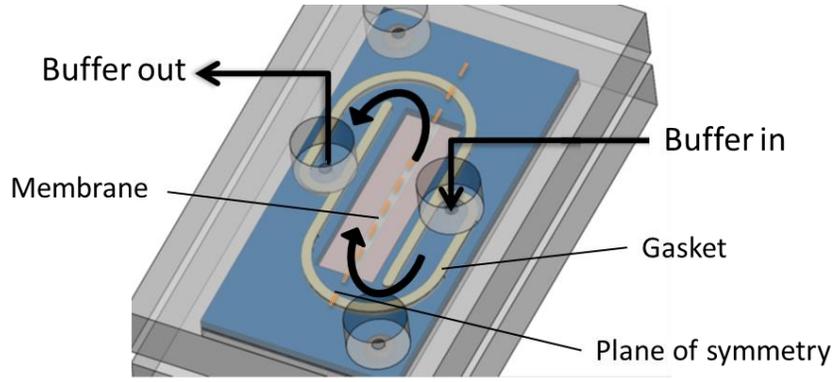
Figure 4.7 Buffer fluid flow path.
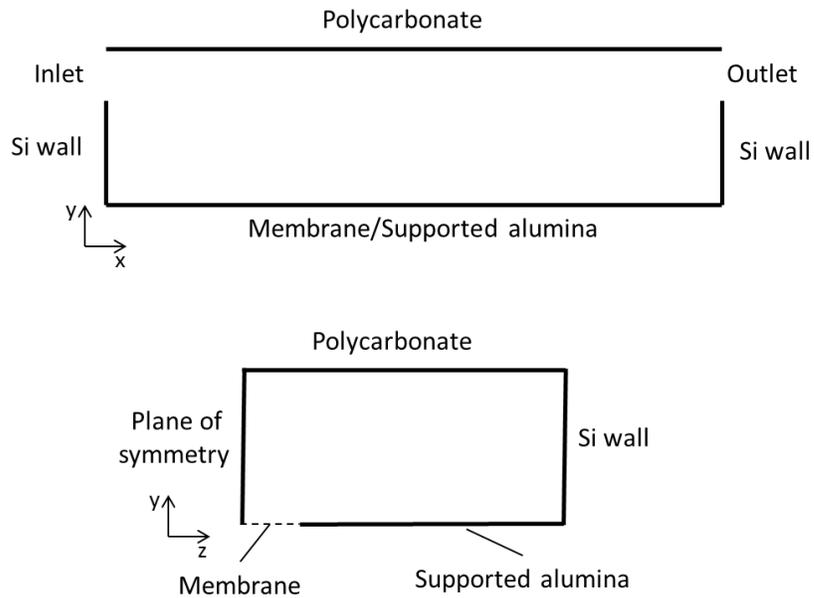
Figure 4.8 shows two cross sections of the three-dimensional domain in which the

governing equations for mass transfer and fluid flow, Equations (4.9) to (4.11), were

discretized and solved simultaneously using COMSOL. The figure also illustrates what

every one of the surfaces is equivalent to in the physical device. All the dimensions were

the same as they were in the final assembly. A plane of symmetry was implemented

along the center of the membrane in order to reduce the domain size and optimize

computational resources. Figure 4.7 shows were this plane is located in the experimental

arrangement.
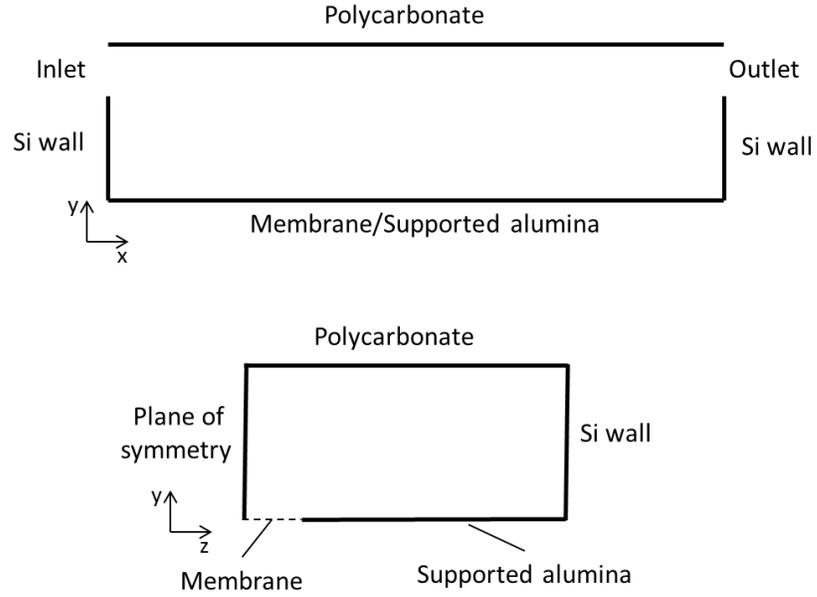
Figure 4.8 Computational simulation domain.

$$\nabla \cdot (-D_i \nabla C_b) + \vec{U} \cdot \nabla C_b = 0 \tag{4.9}$$

$$\rho(\vec{U} \cdot \nabla)\vec{U} = -\nabla P_b + \mu \nabla^2 \vec{U} \tag{4.10}$$

$$\nabla \cdot \vec{U} = 0 \tag{4.11}$$

In these expressions, $\vec{U}$ is the velocity vector, D_i is the free diffusion coefficient of

potassium chloride in water, and ρ is the density of the fluid.

Table 4.1 summarizes the boundary conditions imposed on each of the surfaces based on how they were believed to behave in the physical system. A constant normal inflow velocity with no species concentration was imposed at the inlet. The fluid velocity on this surface was calculated from the known cross sectional area of the inlet and the flow rate used during experiments. At the outlet, a pressure of 0 was assigned, while diffusive transport was ignored. At the symmetry plane no normal fluid velocity and no mass flux were imposed. Since mass transfer boundary conditions at the membrane are not trivial to determine based on the experimental setup, two different scenarios were considered. No-slip condition with a constant concentration, and with a constant mass flux were studied. In the table $\vec{n}$ is the vector normal to the surface.

Table 4.1 Computational model boundary conditions.

Surface	Mass Transfer Boundary Condition	Fluid Flow Boundary Condition
Inlet	$C_b = 0$	$\vec{U} = -0.07\,\vec{n}$ (m/s)
Outlet	$-\vec{n} \cdot (D_i \nabla C_b) = 0$	$P_b = 0$
Membrane	$C_b = 300$ (mol/m^3)	$\vec{U} = 0$
	$-\vec{n} \cdot (D_i \nabla C_b + \vec{U}C) = 0.01$ (mol/m^{2}s)	$\vec{U} = 0$
Plane of symmetry	$-\vec{n} \cdot (D_i \nabla C + \vec{U}C) = 0$	$\vec{U} \cdot \vec{n} = 0$
All other surfaces	$-\vec{n} \cdot (D_i \nabla C + \vec{U}C) = 0$	$\vec{U} = 0$

The local mass transfer coefficient was calculated for every case with Equation (4.12) and averaged over the width of the membrane. The results are plotted along with the two dimensional velocity profile at the symmetry plane. The graph shows that for most of the length, the mass transfer coefficient is changing. Close to the silicon walls located below the inlet and outlets, a small mass transfer coefficient results from the

stagnation of fluid close to the membrane caused by the sudden change in channel geometry.

$$h_b = \frac{-\vec{n} \cdot J''}{C_b - C_\infty}$$ (4.12)

In the equation above C_∞ is the free stream fluid concentration, which was found to have a maximum value in the order of 1E-4 mM under the conditions imposed. This confirms that C_b remains negligibly small during experiments, as assumed in the model.
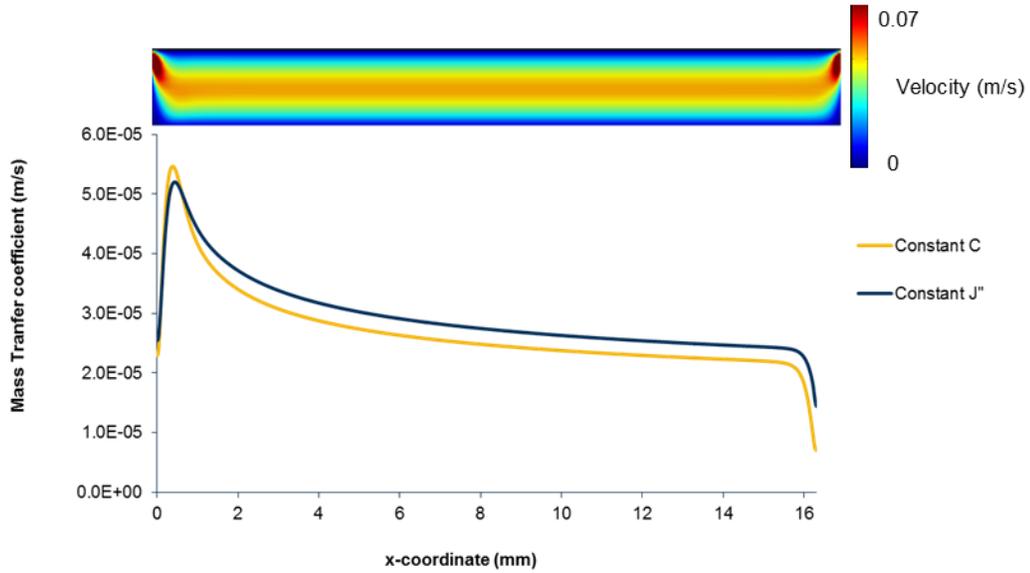

Figure 4.9 Mass transfer coefficient and velocity field.

4.2.3 Analysis of Results

The more rigorous model developed at the beginning of Section 4.2 was solved using the insight obtained from the experimental characterization of the membrane and

the computational determination of the flow properties. The data obtained from testing of

the system performance with the procedure described in Section 4.1.1 was plotted again

against a computational solution of Equations (4.2) to (4.6) in Figure 4.10. The residence

time was calculated from the flow rate at the inlet of the channel in both, the

experimental data and the analytical model.
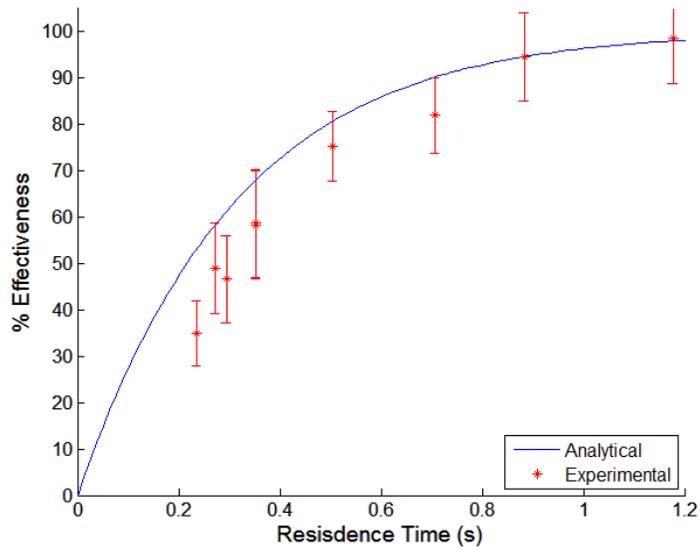

Figure 4.10 Experimental data compared to improved model.

The data and its prediction are in reasonable agreement, which suggests that the

physical principles that govern the MD device are understood. It can be concluded that

the system presented can achieve more than 95% desalting in less than 1.2 seconds,

which indicates success in attaining the goals of this project.

4.3 Mass Spectrometry Analyses

Having demonstrated successful rapid desalting of a solution by concentration measurements, the device's ability to enable the identification of an analyte in a solution with high salt content by ESI-MS was examined.

A mixture of 40 μM cytochrome-c (Cyt-C) in deionized water was prepared and analyzed. Figure 4.11 shows the mass spectrum obtained. Peaks indicate presence this analyte at charge states of +5 to +10 are clearly visible. An optimal desalting system would be able to reproduce this result from a sample that has a high salt content.
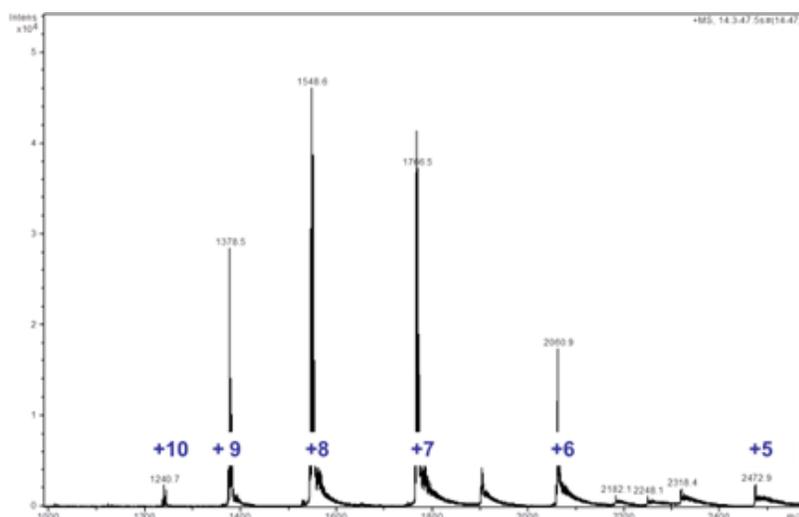
Figure 4.11 ESI-MS mass spectrum of 40 μM Cyt-C.

A solution of 100 mM potassium chloride and 40 μM Cyt-C was then prepared. This mixture was also studied with ESI-MS. As expected, Figure 4.11 shows that the mass spectrum that results from this analysis does not reveal the presence of the analyte of interest. The sample was then treated with the MD system by making it flow through the sample channel of the device at 30 μL/hr, while the buffer fluid flowed at 50 ml/hr, as

in the experiments in Section 4.1.1. The sample was then analyzed again with mass

spectrometry. The result is shown in Figure 4.13. Not all the charge states are visible in

Figure 4.11 are present, which is due, most likely, to incomplete salt removal. However,

the peaks that can be discerned do reveal the presence of the biomolecule, which once

again confirms that the objectives of the project were attained. Recommended strategies

to obtain better results are discussed in the next Chapter.
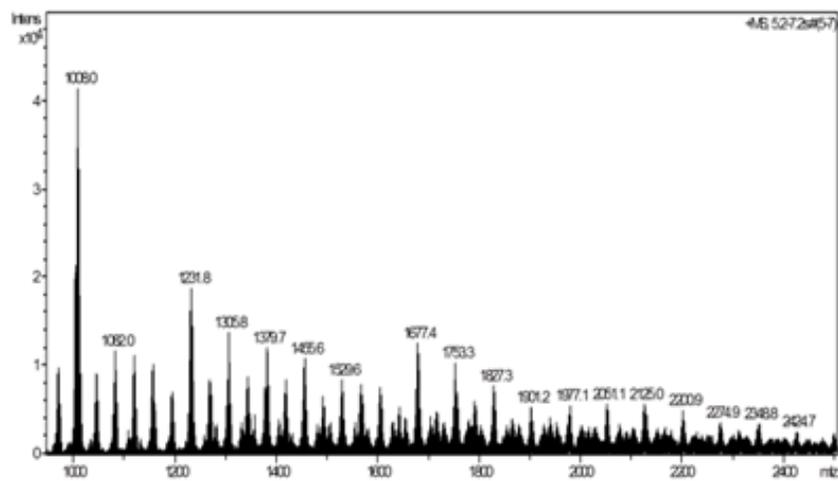

Figure 4.12 Mass spectrum of 40 µM Cyt-C and 100 mM KCl before microdialysis.
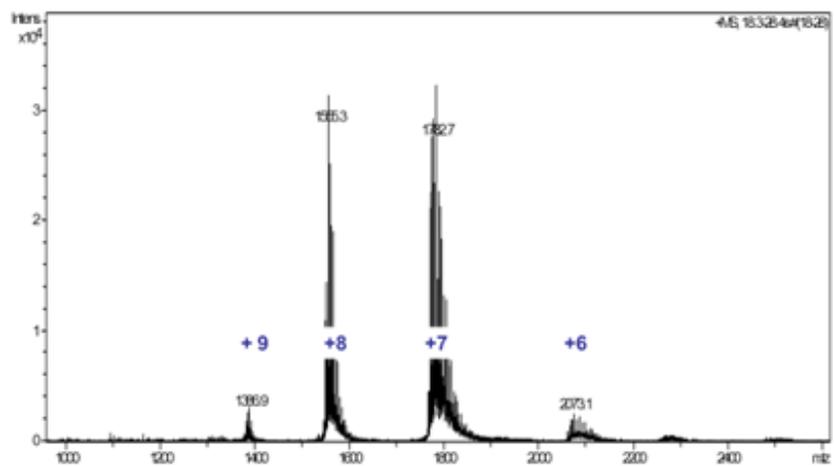
Figure 4.13 Mass spectrum of 40 µM Cyt-C and 100 mM KCl after microdialysis.

CHAPTER 5

CONCLUSIONS AND RECOMMENDED FUTURE WORK

5.1 Conclusions

The Microdialysis (MD) device developed in this thesis is an enabling technology for sample pre-treatment for transient biomolecule identification. It is demonstrated that the device removes more than 95% of salts of a solution flowing at typical electrospray flow rates in less than 1.5 seconds while permitting interfacing with an ion source with a convenient approach. ESI-MS analyses of biomolecules in solution treated with the device confirm the ability of the system to enable their rapid identification with this technique. Longer residence times required by other desalting methods previously reported compromise the ability to dynamically identify transient intermediate products in biological processes.

In order to accomplish this, first, a preliminary analysis of MD was performed. An expression was derived for the salt concentration of a liquid sample as a function of the time it spends in a channel that is separated from a buffer fluid by a porous membrane. By performing a parametric study using this equation, the key features to optimize system performance were identified. Decisions on device geometry were made based on the information collected from this investigation, practical limitations recognized by testing of early prototypes, and consideration of the capabilities of current state of the art microfabrication techniques. An adequate design solution was reached in which a compromise between optimizing performance and facilitating fabrication and

packaging processes was made. As a result, a sample channel of height, width, and length of 5 µm, 100 µm, and 16.3 mm, respectively, separated from a buffer channel of 100 µm hydraulic diameter by a 5 µm porous alumina membrane was deemed as a feasible system design. Such a device was expected to completely remove salts in approximately 0.5 seconds.

The device was subsequently microfabricated mostly using techniques that have been well established by the microelectronics industry. In some cases the specifications of the individual critical steps and the order in which they were performed were determined by iteratively executing the process and finding solutions to problems that may have arisen. The optimal parameters to critical steps of the fabrication were found by performing them in isolation from the rest of the process under different specifications and selecting the ones that yielded the best results. A device resulted that featured a microchannel for sample flow that had transport access to a buffer chamber, which was contained in the package. The lateral walls of the sample channel were defined by SU-8, while a Pyrex substrate constituted the bottom wall. A porous membrane separated the sample from the buffer fluid. This membrane was created with a special procedure for anodizing a layer of aluminum, which created high aspect ratio cylindrical pores 50 nm in diameter and were as long as the thickness of the membrane. The device was packaged with a polycarbonate case that had machined fluidic connections, and sealing was accomplished with laser-cut silicone gaskets and commercial O-rings. Problems that may arise during emulation of the process were anticipated, and recommendations to remedy them were given.

The device was then tested by assessing the change in concentration that a salt solution underwent after being treated with the device. The solution flowed in the sample channel and DI water in the buffer. Different flow rates were used for the sample to assess effectiveness as a function of residence time. The final concentration of the salt solution was measured using a procedure of argentometric titrations, which had been optimized for the purpose of this work to yield the smallest possible error. The dialysis results obtained indicated significantly lower performance than the one predicted by the analysis used to design the device. In consequence, a more rigorous model was created that took into account cross flow across the membrane due to large pressure differences in the channel and the effect that the uncommon geometry of the buffer channel may have had on mass transfer resistance. Considering these factors accomplished a more successful prediction of the data, which demonstrated more than 95% salt removal in less than 1.2 seconds.

Finally, the device was used to remove salts from a sample of dissolved cytochrome c (Cyt-C). ESI-MS of the sample prior to being treated, resulted in a mass spectrum from which no peaks that revealed presence of the biomolecule could be discerned. After desalting with the MD device with a residence time of 1.2 seconds, four peaks corresponding to four charge states of Cyt-C were seen in the mass spectrum, which confirmed the effectiveness of the device. However, a different mixture of the same concentration of Cyt-C but no salt content had yielded a mass spectrum with visible peaks corresponding to six charged states. This indicates that there is room for improvement in the MD system.

5.2 Recommended Future Work

Even though the MD device demonstrates rapid desalting, in order to keep transit time between sampling and analysis to a minimum during analysis, the MD device must be interfaced with an electrospraying tip efficiently. The fabrication process and the geometry of the device presented in this thesis enable the fulfillment of this requirement. A tip like the one previously designed by Arscott et al. [13] can be conveniently implemented. As shown in Figure 5.1, such a tip could consist of two triangular SU-8 structures protruding from the edge of the substrate that are separated by a small gap. Comparison with the MD device presented in this work shows that the same packaging concept presented in Chapter 3 can be used.
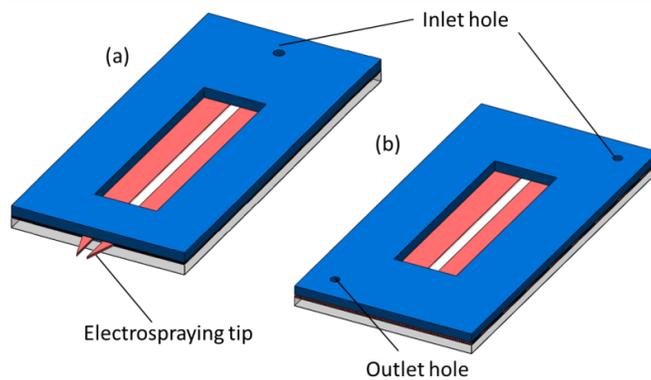

Figure 5.1 Microdialysis device (a) with and (b) without integrated tip (not to scale).
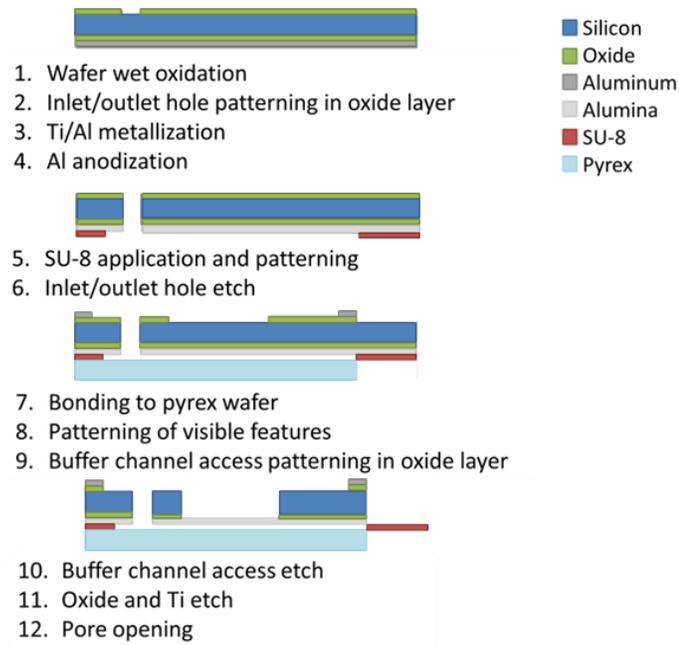
Figure 5.2 Suggested process flow for electrospray tip integration into MD device.

As depicted in Figure 5.2 above, the same process flow used to fabricate the microdialysis device could be used to integrate these tips. For the most part, only a different set of masks for photolithography would be required. The main challenge to overcome would be the release of the fragile free-standing SU-8 structures from the Pyrex and silicon substrates, but even some progress was made towards this end during this work.

It was found that release from the Pyrex substrate can be very simple. A groove 400 μm in depth was made with a dicing saw where the tip was intended to be released before cutting the wafer to separate individual devices. Then, by forcing a razor between it and the silicon substrate in every device, the Pyrex on the tip was easily removed without affecting the SU-8 structure.

Removal of silicon, on the other hand, proved to be significantly more challenging. The possibility of etching it with the same parameters as the buffer channel access after the Pyrex had been removed was investigated. The tips had to be protected with a layer of photoresist in order to not expose them to the gases in the chamber. Due to substrate heating, this protection layer became difficult to remove without damaging the structures once the etch was completed. A promising approach to attempt next would be to remove the alumina layer, and perhaps the oxide underneath it, with a wet etch. This would possibly detach the tip from the silicon and an approach similar to that of the Pyrex side can then be used.

The microdialysis device also has a potential to further reduce sample residence time by implementing some improvements. The Pyrex substrate, for instance, can be replaced by a second silicon substrate on which a porous alumina layer has also been processed. A second buffer access can then be etched with the same parameters as the first one. This improvement would not only increase salt removal rate from the sample by diffusion, but it would also enable electrical migration of species, which could, in theory, significantly accelerate mass transport. This can be achieved by applying an electric field orthogonal to direction of sample flow with electrodes included in the package. These additions can further improve the time and effectiveness of dialysis and present intriguing opportunities for future studies.

REFERENCES

[1]   J. P. Kutter, "Current developments in electrophoretic and chromatographic separation methods on microfabricated devices," *TrAC Trends in Analytical Chemistry,* vol. 19, pp. 352-363, 2000.

[2]   A. Manz, D. J. Harrison, E. M. Verpoorte, J. C. Fettinger, A. Paulus, H. Lüdi*, et al.*, "Planar chips technology for miniaturization and integration of separation techniques into monitoring systems: capillary electrophoresis on a chip," *Journal of Chromatography A,* vol. 593, pp. 253-258, 1992.

[3]   R. B. Cole, *Electrospray Mass Spectrometry—Fundamentals, Instrumentation and Application*: John Wiley: New York, 1997.

[4]   P. A. Kottke, F. L. Degertekin, and A. G. Fedorov, "Scanning mass spectrometry probe: a scanning probe electrospray ion source for imaging mass spectrometry of submerged interfaces and transient events in solution," *Analytical chemistry,* vol. 82, pp. 19-22, 2009.

[5]   N. B. Cech and C. G. Enke, "Practical implications of some recent studies in electrospray ionization fundamentals," *Mass Spectrometry Reviews,* vol. 20, pp. 362-387, 2001.

[6]   D. J. Wilson and L. Konermann, "A capillary mixer with adjustable reaction chamber volume for millisecond time-resolved studies by electrospray mass spectrometry," *Analytical chemistry,* vol. 75, pp. 6408-6414, 2003.

[7]   D. J. Wilson, S. P. Rafferty, and L. Konermann, "Kinetic unfolding mechanism of the inducible nitric oxide synthase oxygenase domain determined by time-resolved electrospray mass spectrometry," *Biochemistry,* vol. 44, pp. 2276-2283, 2005.

[8]   D. Olivero, "Traumatic brain injury biomarker discovery using mass spectrometry imaging of 3D neural cultures," Master of Science, School of Mechanical Engineering, Georgia Institute of Technology, 2011.

[9]   D. P. H. Smith, "Electrohydrodynamic Atomization of Liquids," *IEEE Transactions on Industry Applications,* vol. IA-22, pp. 527-535, 01 / 01 / 1986.

[10]   G. A. Schultz, T. N. Corso, S. J. Prosser, and S. Zhang, "A fully integrated monolithic microchip electrospray device for mass spectrometry," *Analytical Chemistry,* vol. 72, pp. 4058-4063, 09 / 01 / 2000.

[11]   W. Kim, P. Yang, M. Guo, and D. Wang, "Microfabricated monolithic multinozzle emitters for nanoelectrospray mass spectrometry," *Analytical Chemistry,* vol. 79, pp. 3703-3707, 05 / 15 / 2007.

[12]   R. Ramsey and J. Ramsey, "Generating electrospray from microchip devices using electroosmotic pumping," *Analytical Chemistry,* vol. 69, pp. 1174-1178, 1997.

[13]   S. Arscott, C. Druon, P. Tabourier, S. Le Gac, and C. Rolando, "Micromachined 2D nanoelectrospray emitter," *Electronics Letters,* vol. 39, pp. 1702-1703, 11 / 27 / 2003.

[14]   J. Carlier, S. Arscott, V. Thomy, J.-C. Camart, C. Cren-Olivé, and S. Le Gac, "Integrated microfabricated systems including a purification module and an on-chip nano electrospray ionization interface for biological analysis," *Journal of Chromatography A,* vol. 1071, pp. 213-222, 2005.

[15]   A. Apffel, J. A. Chakel, S. Fischer, K. Lichtenwalter, and W. S. Hancock, "Analysis of oligonucleotides by HPLC-electrospray ionization mass spectrometry," *Analytical chemistry,* vol. 69, pp. 1320-1325, 1997.

[16]   K. Bleicher and E. Bayer, "Analysis of oligonucleotides using coupled high performance liquid chromatography-electrospray mass spectrometry," *Chromatographia,* vol. 39, pp. 405-408, 1994.

[17]   J. Cavanagh, R. Thompson, L. M. Benson, and S. Naylor, "In-line desalting mass spectrometry for the study of noncovalent biological complexes," *Analytical Chemistry,* vol. 75, pp. 3281-3286, 07 / 15 / 2003.

[18]   M. L. Shen, L. M. Benson, K. L. Johnson, J. J. Lipsky, and S. Naylor, "Effect of enzyme inhibitors on protein quaternary structure determined by on-line size exclusion chromatography-microelectrospray ionization mass spectrometry," *Journal of the American Society for Mass Spectrometry,* vol. 12, pp. 97-104, 2001.

[19]   A. Deroussent, J. P. Le Caer, J. Rossier, and A. Gouyette, "Electrospray mass spectrometry for the characterization of the purity of natural and modified oligodeoxynucleotides," *Rapid communications in mass spectrometry : RCM,* vol. 9, pp. 1-4, 01 / 01 / 1995.

[20]   C. G. Huber and M. R. Buchmeiser, "On-line cation exchange for suppression of adduct formation in negative-ion electrospray mass spectrometry of nucleic acids," *Analytical chemistry,* vol. 70, pp. 5288-5295, 1998.

[21]   C. Liu, Q. Wu, A. C. Harms, and R. D. Smith, "On-Line Microdialysis Sample Cleanup for Electrospray Ionization Mass Spectrometry of Nucleic Acid Samples," *Analytical Chemistry,* vol. 68, pp. 3295-3299, 1996/01/01 1996.

[22]   Q. Wu, C. Liu, and R. D. Smith, "On-line microdialysis desalting for electrospray ionization-mass spectrometry of proteins and peptides," *Rapid Communications in Mass Spectrometry,* vol. 10, pp. 835-838, 01 / 01 / 1996.

[23]   L. Sun, J. Duan, D. Tao, Z. Liang, W. Zhang, L. Zhang*, et al.*, "A facile microdialysis interface for on-line desalting and identification of proteins by nano-electrospray ionization mass spectrometry," *Rapid Communications in Mass Spectrometry,* vol. 22, pp. 2391-2397, 2008.

[24]   E. S. M. Lutz and M. Larsson, "On-line microdialysis-electrospray mass spectrometry for automated desalting of small-volume peptide samples," *Chromatographia,* vol. 49, pp. S28-S34, 01 / 01 / 1999.

[25]   D. C. Muddiman, D. S. Wunschel, C. Liu, L. Paša-Tolic, K. F. Fox, A. Fox*, et al.*, "Characterization of PCR products from bacilli using electrospray ionization FTICR mass spectrometry," *Analytical Chemistry,* vol. 68, pp. 3705-3712, 1996.

[26]   J. A. Jakubowski, N. G. Hatcher, and J. V. Sweedler, "Online microdialysis-dynamic nanoelectrospray ionization-mass spectrometry for monitoring neuropeptide secretion," *Journal of Mass Spectrometry,* vol. 40, pp. 924-931, 07 / 01 / 2005.

[27]   D. Olivero, M. LaPlaca, and P. A. Kottke, "Ambient Nanoelectrospray Ionization with In-Line Microdialysis for Spatially Resolved Transient Biochemical Monitoring within Cell Culture Environments," *Analytical Chemistry,* vol. 84, pp. 2072-2075, 02/21/ 2012.

[28]   N. Xu, Y. Lin, S. A. Hofstadler, D. Matson, C. J. Call, and R. D. Smith, "A Microfabricated Dialysis Device for Sample Cleanup in Electrospray Ionization Mass Spectrometry," *Analytical Chemistry,* vol. 70, pp. 3553-3556, 09 / 01 / 1998.

[29]   F. Xiang, Y. Lin, J. Wen, D. W. Matson, and R. D. Smith, "An integrated microfabricated device for dual microdialysis and on-line ESI-ion trap mass spectrometry for analysis of complex biological samples," *Analytical Chemistry,* vol. 71, pp. 1485-1490, 1999.

[30]   R. K. Shah, "Laminar flow forced convection in ducts," *Advances in Heat Transf.,* 1978.

[31]   S. Narayanan, A. G. Fedorov, and Y. K. Joshi, "On-chip thermal management of hotspots using a perspiration nanopatch," *Journal of Micromechanics and Microengineering,* vol. 20, 01 / 01 / 2010.

[32]   R. W. Fox, A. T. McDonald, and P. J. Pritchard, *Introduction to fluid mechanics* vol. 5: John Wiley & Sons New York, 1998.

[33]   F. P. Incropera, D. P. Dewitt, T. L. Bergman, and A. S. Lavine, *Introduction to heat transfer*: John Wiley & Sons, 2011.